ERDC TR-19-7

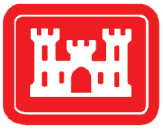

US Army Corps
of Engineers®
Engineer Research and
Development Center

Numerical Simulation of Biological Structures

Paddlefish Rostrum

Felipe J. Acosta, Guillermo A. Riveros, Reena R. Patel,
and Wayne D. Hodo

May 2019

Approved for public release; distribution is unlimited.

Engineer Research and
Development Center

The U.S. Army Engineer Research and Development Center (ERDC) solves the nation's toughest engineering and environmental challenges. ERDC develops innovative solutions in civil and military engineering, geospatial sciences, water resources, and environmental sciences for the Army, the Department of Defense, civilian agencies, and our nation's public good. Find out more at www.erdc.usace.army.mil.

To search for other technical reports published by ERDC, visit the ERDC online library at http://acwc.sdp.sirsi.net/client/default.

ERDC TR-19-7
May 2019

Numerical Simulation of Biological Structures

Paddlefish Rostrum

Guillermo A. Riveros and Reena R. Patel

Information Technology Laboratory
U.S. Army Engineer Research and Development Center
3909 Halls Ferry Road
Vicksburg, MS 39180-6199

Wayne D. Hodo

Geotechnical and Structures Laboratory
U.S. Army Engineer Research and Development Center
3909 Halls Ferry Road
Vicksburg, MS 39180-6199

Felipe J. Acosta

University of Puerto Rico-Mayaguez
Department of Civil Engineering and Surveying
PO Box 9000
Mayagüez PR 00681-9000

Final report

Approved for public release; distribution is unlimited.

Prepared for U.S. Army Corps of Engineers
Washington, DC 20314-1000

Under Work Unit AR058

Abstract

The rostrum of a paddlefish is used as an antenna to detect electrostatic impulses emitted by plankton and also for hydrodynamic stability while feeding. The rostrum is formed by a network of cartilage, tissue, and interlocking star-shaped bones called stellate bones. The objective of this work is to study the load transfer mechanisms of the rostrum bone structure. Steel with elastic-plastic behavior is considered in this study as a basic homogeneous material to evaluate the performance of four models using the following elements: first-order reduced integration, first-order full integration, second-order reduced integration, and second-order full integration. From the study is found that second-order formulation resulted in lower structural stiffness as seen by higher displacements and stresses than using first-order formulated elements. Von Mises stresses and global stresses along the rostrum and at a particular location as well as bones were extracted and compared for the second-order-reduced integration model.

DISCLAIMER: The contents of this report are not to be used for advertising, publication, or promotional purposes. Citation of trade names does not constitute an official endorsement or approval of the use of such commercial products. All product names and trademarks cited are the property of their respective owners. The findings of this report are not to be construed as an official Department of the Army position unless so designated by other authorized documents.

DESTROY THIS REPORT WHEN NO LONGER NEEDED. DO NOT RETURN IT TO THE ORIGINATOR.

Contents

Figures and Tables

Figures

Tables

Preface

This study was conducted for the Military Engineering 6.1 Basic Research Program under Project WP # 17-202, "Complex Network Analysis for Early Detection of Failure Mechanisms in Resilient Biostructures." The technical monitor was Dr. Edward J. Perkins of the U.S. Army Engineer Research and Development Center, Environmental Laboratory (ERDC-EL).

The work was performed by the Computational Analysis Branch (CAB) of the Computational Science and Engineering Division (CSED), Information Technology Laboratory (ERDC-ITL), and the Geotechnical and Structural Laboratory, (ERDC-GSL). At the time of publication, Dr. Jeffery L. Hensley was Chief, CEERD-IE-C; Dr. Jerrell R. Ballard was Chief, CEERD-IE; and Mr. David R. Richards was the Technical Director for Engineering and Science. The Deputy Director of ERDC-ITL was Ms. Patti S. Duett and the Director was Dr. David Horner.

COL Ivan P. Beckman was the Commander of ERDC, and Dr. David W. Pittman was the Director.

Unit Conversion Factors

Multiply	By	To Obtain
cubic feet	0.02831685	cubic meters
cubic inches	1.6387064 E-05	cubic meters
feet	0.3048	meters
foot-pounds force	1.355818	joules
gallons (U.S. liquid)	3.785412 E-03	cubic meters
inches	0.0254	meters
inch-pounds (force)	0.1129848	newton meters
ounces (mass)	0.02834952	kilograms
ounces (U.S. fluid)	2.957353 E-05	cubic meters
pounds (force)	4.448222	newtons
pounds (force) per foot	14.59390	newtons per meter
pounds (force) per inch	175.1268	newtons per meter
pounds (force) per square foot	47.88026	pascals
pounds (force) per square inch	6.894757	kilopascals
pounds (mass)	0.45359237	kilograms
pounds (mass) per cubic foot	16.01846	kilograms per cubic meter
pounds (mass) per cubic inch	2.757990 E+04	kilograms per cubic meter
pounds (mass) per square foot	4.882428	kilograms per square meter
pounds (mass) per square yard	0.542492	kilograms per square meter
slugs	14.59390	kilograms
square feet	0.09290304	square meters

1 Introduction

1.1 Background

Nature produces biological structures that have evolved by billions of years in a way that their mechanical properties are extraordinary. Some examples are oyster shells, bones, fish scales, and spider webs, among others. Scientists have had a special interest in studying these systems to understand the relationship that exist between these lightweight compound materials and at the same time highly strong to develop man-made materials with similar properties and behaviors (Sen 2011; Flammang and Porter 2011; Allison et al. 2013a; Vepari and Kaplan 2007).

The paddlefish (Polyodon spathula) is native to the Mississippi River basin in the U.S. (Beach 1902) (Figure 1). It is characterized for having a flat pallet rostrum almost one-third of its body length. The rostrum of paddlefish has a unique structure formed by a network of cartilage, tissue, and interlocking star-shaped bones called stellate bones. Figure 2 shows the bone structure in the rostrum of a paddlefish. It has been found that the rostrum acts as antenna to detect electromagnetic signals (Gurgens et al. 2000; Wilkens et al. 2002; Wilken and Hofmann 2007; Hoover et al. 2013b). It also provides hydrodynamics stability during feeding in adults (Meyer 1960, Spargue 1959). Paddlefish swim with their mouths wide open during filter feeding and take in enormous amounts of water. The paddle allow the fish to swim straight and fast to increase the food intake (Patel and Riveros 2013; Hoover et al. 2013a; Hoover et al. 2013b; Allen and Riveros 2013).

Figure 1. North America paddlefish.

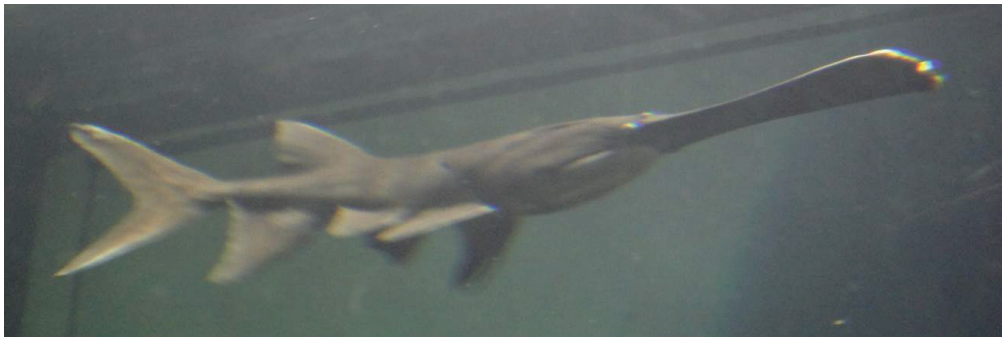

Figure 2. Stellate bone arrangement in the rostrum of paddlefish.

1.2 Challenges in modeling biological structures

Finite element modeling (FEM) of biological structures brings challenges that must be carefully addressed. These challenges are: generation of the geometry (i.e., from CT scan image to solid for meshing) (McCurry et al. 2015), element mesh density and element types (Bright and Rayfield 2011, Tseng et al. 2011; Dumont et al. 2005), element connectivity (i.e. tissues with bone and cartilages) (Cheung et al. 2005; Yu et al. 2008;), loads and displacements boundary conditions (Dumont et al. 2005), and material behavior (Freutel et al. 2014; Cheung et al. 2005). Each of these issues can be addressed as the modeling process progresses and some of them, such as determine the appropriate material behavior, demand deep knowledge of the constitutive material behavior and model calibration. This study is a first step to solve the issue of the appropriate element type, keeping the mesh density and material constant.

1.3 Objectives

This report presents an effort to perform a numerical simulation of the mechanical behavior of a paddlefish rostrum using finite element analysis technique, addressing the determination of the appropriate element formulation that better represents the internal structure stress distributions. Finite element modeling is a practical tool that allows detail representation of the paddlefish rostrum, and at the same time has the flexibility to parametrically study its behavior. In this report, four finite element models of a paddlefish rostrum are compared. Each model has the same mesh size composed of tetrahedral and hexahedral solid elements, but each model uses either first-order (linear) elements, or second-order (quadratic) elements formulating the stiffness matrix with reduced or full integration to compare the accuracy of each type of analysis. Results are expressed in terms of the overall behavior and by comparing von Mises and localized stresses along the direction of selected stellate bones. The material used for the study is a grade 345 steel with elastic-plastic

behavior. The model is fixed supported around the rostrum edges and at the fish end and a constant pressure is applied simulating fixed plate behavior. Nonlinear geometry is also considered in the analysis.

2 FEM Models

2.1 Selection between full- and reduced-integration

Reduced integration procedure uses a lower integration quadrature order to form the element stiffness matrix. The integration points are defined by the quadrature rule and are the locations where the strain and stresses are calculated. Stresses at these points are extrapolated to the nodes and surfaces of the elements. In terms of computation time and output file size, reduced integration has the advantage of reducing running time, especially in three-dimensional problems, by approximately 70 percent. Also file size can be reduced proportionally, depending on the type of analysis. Regarding mechanical behavior, reduced integration solve the over stiffening of first-order elements when trying to represent bending. Figure 3 shows the effect of using a first-order quadrilateral element to represent pure bending. The first-order quadrilateral element has four nodes, each with two degrees of freedom (u_i, v_i) (Figure 3a). The element representation of pure bending (Figure 3c) cannot represent the appropriate curvature (Figure 3b), numerically producing shear deformation $\gamma_{xy} \neq 0$. The strain vector for the displacement mode in Figure 3c is expressed by:

$$\begin{Bmatrix} \epsilon_x \\ \epsilon_y \\ \gamma_{xy} \end{Bmatrix} = [B][-u, 0, u, 0, -u, 0, u, 0]^T = \begin{Bmatrix} -uy/ab \\ 0 \\ -ux/ab \end{Bmatrix} \quad (1)$$

where:

ϵ_x = strain along the x-axis
ϵ_y = strain along the y-axis
γ_{xy} = shear strain in the x-y plane
$[B]$ = $[\partial][N]$, a 3 x 6 matrix of the partial derivatives of the displacement shape functions
a, b = half dimension of each element side
x, y = coordinates along the x- and y- axes
u = displacement along the x-axis

In the Equation 1, the final value of γ_{xy} is an expression that linearly varies in x. The results is a “saw tooth”-like curve. The artificially produced shear strain energy penalizes the total strain energy field, producing the shear locking of the element. It is translated on elements that are stiffer than are

supposed to be, showing lower displacement values in bending. This behavior also manifests in first-order brick elements. A disadvantage of using reduced integration is that in particular cases based on loading and displacement boundary condition, the mesh might produce deformations that coincide with certain "zero energy" modes or hourglass modes. This problem is overcome as the mesh is refined and loaded, and boundary conditions are applied to restrain or not to provoke such modes.

Figure 3. First-order quadrilateral element: (a) general dimensions, nodes and degrees of freedom per node, (b) representation of a beam segment in pure bending, (c) displacements of the element in pure bending (Cook et al. 2002).

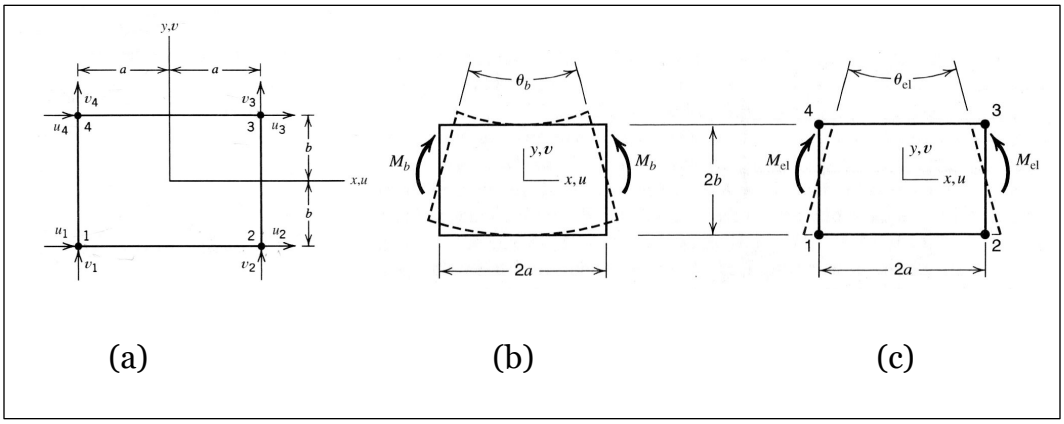

2.2 Model description

A finite element mesh was constructed and imported to ABAQUS software from a tomography (CT scan) of the actual paddlefish rostrum. Based on the gray tones of the scanned image caused by the difference in material densities, three principal parts can be identified: primary cartilage (Figure 4 and 5(a)) that includes the central and side stellate bones, secondary or central cartilage (Figure 5b), and the tissue (Figure 5c). There is a fourth category in the actual rostrum that has jelly type behavior but it was not included in this part of the study. These different components of the rostrum were also experimentally identified after performing nanoindentation and tension/compression tests on the main bones and cartilages (Allison et al. 2013b; Deang et al. 2017). In Allison et al. (2013b) through nanoindentation was found that the middle bone (hard cartilage)'s average elastic modulus measured was 12.06 GPa. Properties of the stellate bones varied, with peak values similar to the center bone. Deang et al. (2017) performed several compression and tension tests on the central cartilage (secondary cartilage). Because this constituent behaves as a hyperelastic material, the tests were performed evaluating its response at different strain

rates. Results were later fitted to an Ogden hyperelastic model to use with the finite element analyses. The tissue part not only includes the exterior surface, but it also comprises the material that encases the hard and secondary cartilages. The secondary cartilage runs along the longitudinal direction of the rostrum (z-axis) of the model and constitutes the center portion of the rostrum (Figure 6). The primary cartilage, shown in Figure 4a and Figure 4b, is formed by two flat sections that run along the longitudinal axis too and branches out from the center in a form of a truss-like structure to the full width of the rostrum. These truss-like structures are joined together at their ends around the rostrum edges. These three parts are individually meshed in ABAQUS by a combination of tetrahedral and hexahedral solid elements for a total of 1,420,163 elements, where 119,712 are hexahedral (C3D8 for first-order or C3D20 for second-order), and 1,300,451 are tetrahedral (C3D4 for first-order or C3D10 for second-order). The total number of equations to solve are 1,123,083 for the first-order model and 7,319,172 for the second-order model. Only the hexahedral elements used in these models can be selected to be formulated by a reduced or a full integration. The integration order is defined by the terms used in the quadrature rule to form the elements stiffness matrix, and its advantage and disadvantages were briefly discussed in a previous section. Figure 5 shows the FEM mesh for each of the three components (a) primary cartilage, (b) secondary cartilage, (c) tissue and (d) for the complete assemblage.

Figure 4. Detail of the primary cartilage: (a) overall architecture, (b) cross-sectional cut.

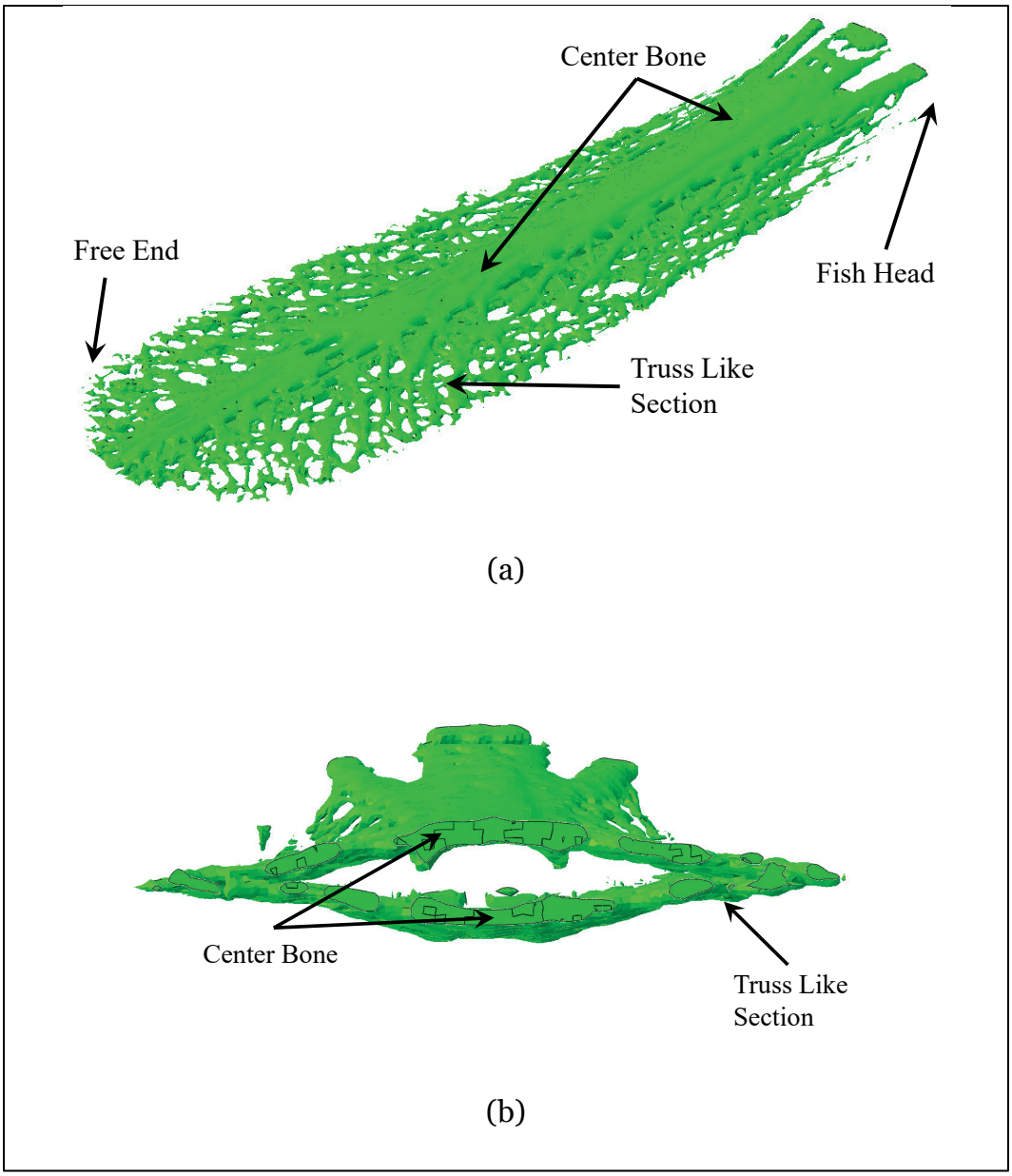

Figure 5. FEM mesh: (a) primary cartilage, (b) secondary cartilage, (c) tissue, and (d) full assemblage.

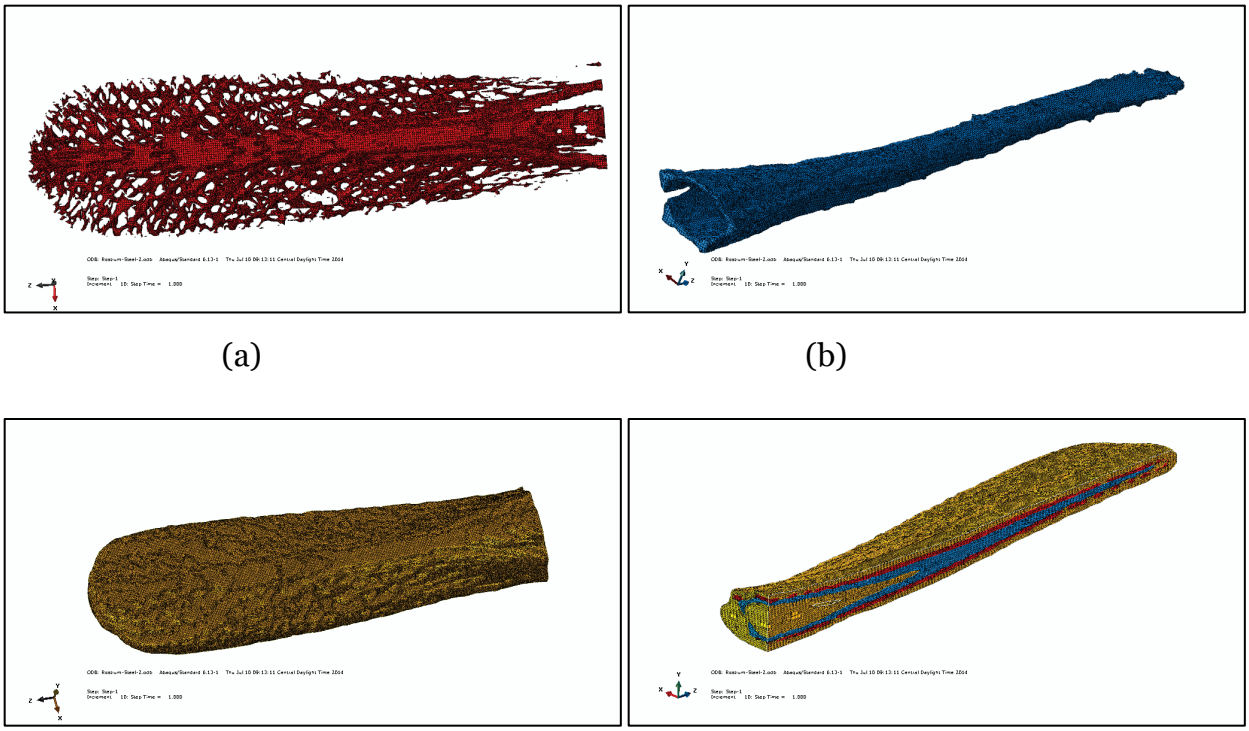

(a) (b)

(c) (d)

Figure 6. Reference axes for the rostrum FEM.

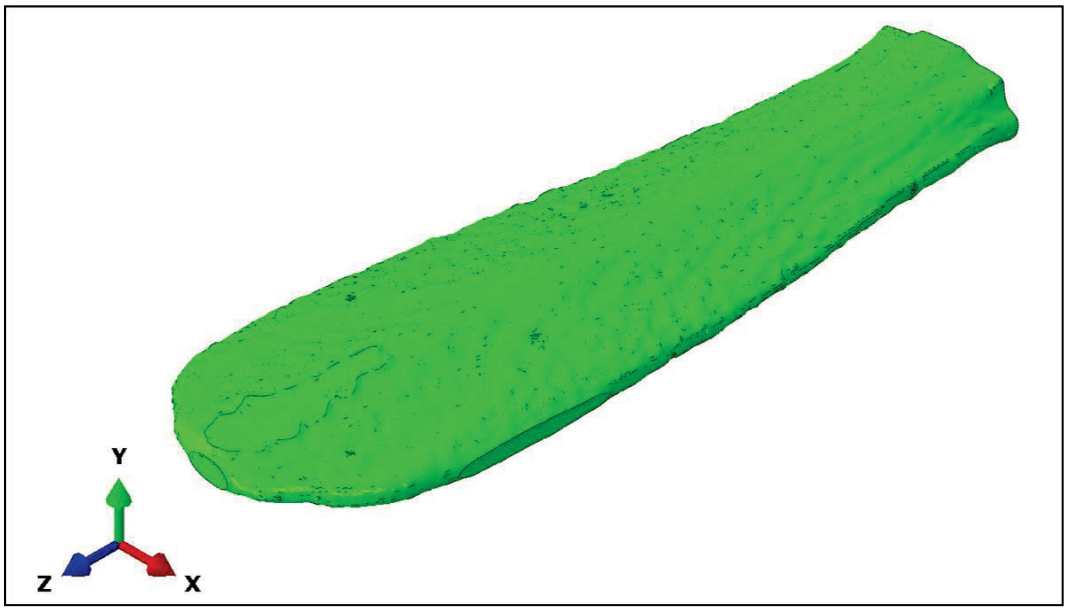

Since the three components are constituted of materials with different hardness and stiffness, the FEM model must be composed of three principal materials. However, to first evaluate the adequacy of the different options of element selection for the rostrum, steel with elastic-plastic behavior was used. The models were subjected to its self-weight and a uniform pressure force over the top surface (see Figure 6 for reference axes).

2.3 Elastic-plastic behavior of steel

To be able to evaluate the four models for the adequate element type and integration scheme to use for the paddlefish, steel was considered as an alternative to examine the response of the rostrum to uniform pressure. It is a well-known material, easing the identification of stress distributions inside the structure. The basic material properties used in the model for steel are shown in Table 1. The table shows the elastic modulus, Poisson's ratio, yield stress, ultimate stress and density. An elastic-plastic model was used to perform a nonlinear analysis of the rostrum structure. Figure 7 shows the elastic-plastic curve for steel. The ultimate stress is 545 MPa. ABAQUS uses plastic curve in the form of true stress and true plastic strain (ABAQUS 2014). Beyond ultimate stress, the model assumes perfectly plastic behavior. ABAQUS uses modulus and Poisson's ratios for the elastic part of the curve. Then, the elastic part of the curve is tabulated from the yield point on by the true yield stresses and plastic strains (not total strain).

Table 1. Material data for grade 345 steel.

Property	SI	US
Elastic modulus	200,000 MPa	29,000,000 psi
Poisson's ratio	0.3	0.3
Yield stress	345 MPa	50,000 psi
Yield strain	0.17%	0.17%
Ultimate tensile stress	545 MPa	79,000 psi
Ultimate strain	20%	20%
Density	7,850 kg/m^3	490 lb/ft^3

Figure 7. Elastic-plastic stress-strain curve for grade 345 steel.

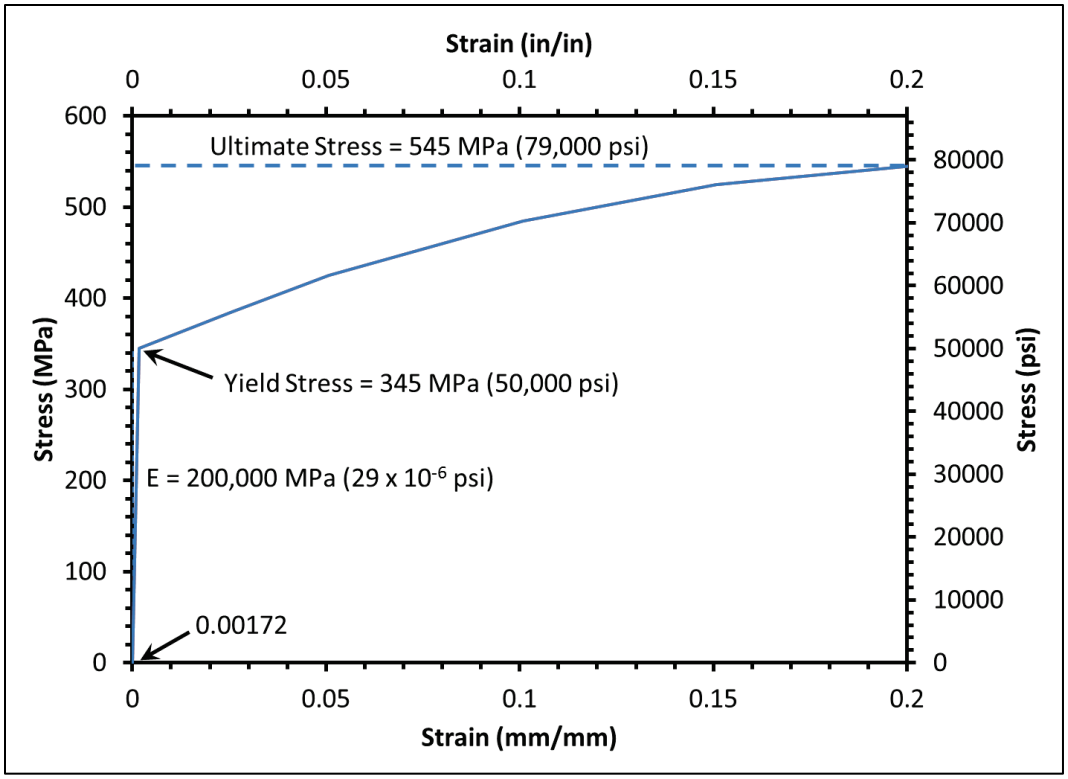

2.4 Displacement and load boundary conditions

The load boundary conditions consisted of a uniform pressure of 25 MPa (3,626 psi) applied over a defined surface on top of the mesh. The pressure forces by definition is applied perpendicular to each element face over the applied zone, thus following the surface contour. This force is represented by the purple arrows shown in Figure 8. Additionally, self-weigh was also included by defining the mass density and the gravity acceleration of 9.807 m/s^2 (32.18 ft/s^2) and applying it to the entire model. The total weight of the model is 18.58 N (4.18 lb), which is insignificant compared with the applied pressure forces.

Figure 8. Loads and boundary conditions of fixed supported model.

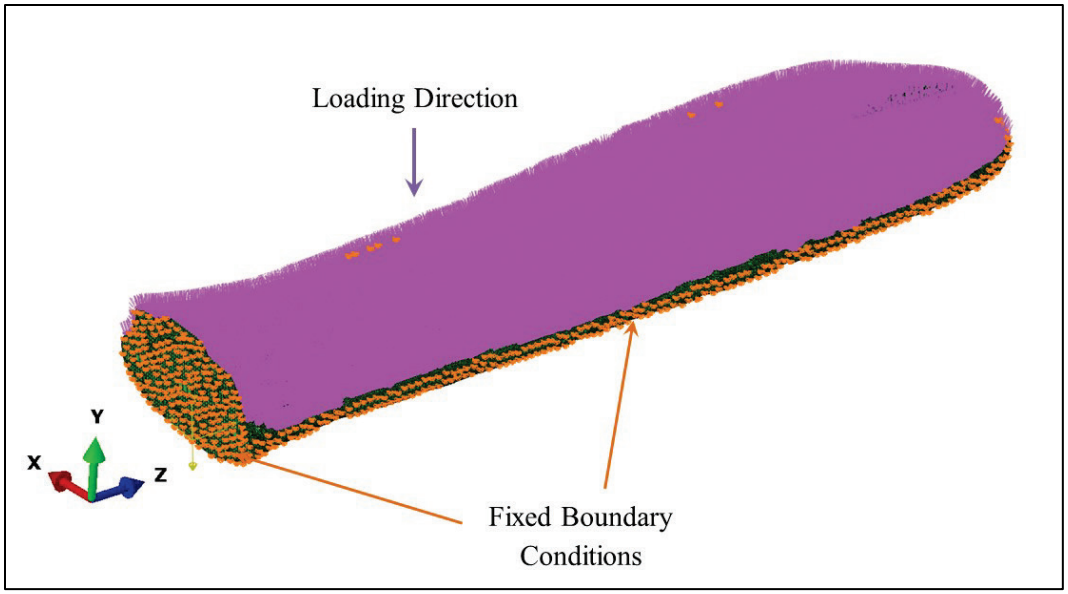

Displacement boundary conditions in the three principal directions (x, y, z) were defined around the edges of the rostrum, applied to several lines of nodes to simulate fixed condition. This type of boundary condition helped to reduce irregular stress concentrations around the edges of the rostrum that are produced if simple boundary conditions are used. Also the model does not have a uniform distributed line of nodes round the borders to be able to define a smooth simple supported supports. Similarly, the three principal directions were restrained for all the nodes located at the back of the rostrum, where the rostrum is attached to the fish head, to simulate fixed support. Since the elements used do not consider rotational degrees of freedom, it is sufficient to just restrain displacements.

2.5 Analysis type

A general quasi-static analysis was performed to the models. Two steps were used. The first step applies only the gravity (self-weigh) load and it is applied in a single increment. Then the pressure force is incrementally applied starting at 0.008 up to a maximum time increment of 0.05 until the total time step of 1.0 is reached. Geometry nonlinearity was also considered in the analysis because high deformations are expected. The load applied at each time increment is the total load multiplied by the respective time increment fraction. Because of the complexity of the analysis, each job was executed using parallel processing capabilities of the U.S. Army Engineer Research and Development Center (ERDC) High Performance Computing facilities. Each job was submitted using 16 cores of a single node (36 cores/node and 116 GBytes of RAM) of Topaz system.

3 Discussion of Results – Global Behavior

3.1 Displacements and yielding

Results were extracted from the FE model at the loading increments where each of the principal parts started to show yielding based on the Von Mises stresses. Von Mises stresses are equivalent tensile stresses derived from the stress deviator (Lubliner 1990; ABAQUS 2014). Pressures and displacements at which each part started to exceed the yield strength (345 MPa) are reported in Table 2. The first column at the left side of Table 2 indicates the rostrum component. The following column indicates the value shown and unit (pressure and displacement). The following columns report pressure and displacement values of each of the four models. The last row reports the maximum displacement achieved at the end of the analysis with the maximum pressure of 25 MPa. Results for both of the first degree models at the secondary cartilage are for the maximum applied pressure. These models did not reach yielding at the secondary cartilage. Since it is a nonlinear analysis (geometrical and material), change in displacements at each load increment is not proportional.

Figure 9 shows a comparison of maximum displacements at each load increment for all models of the rostrum. The beginning of yielding of each component was established setting a limit of 345 MPa (yield stress) to the ABAQUS stress contour plots, generating a light gray when the model shows stresses beyond this value. Values for both first-order and second-order models are almost identical. It was observed that the second-order formulation models showed higher displacement compared to the first-order formulation models. The difference starts to increase once yielding is occurring at approximately 6 MPa. In both cases the full integration produces slightly less displacement than the reduced integration. Meshes with first-order elements converge at a lower ratio than meshes with second-order elements as shown by Benzley et al. (1995) and de Oliveira and Sundness (2016). Displacements of the full integration models are 2.65 percent and 3.83 percent lower than the reduced integration models for first-order and second-order formulations, respectively. Displacements of the second-order formulated models are 95.82 percent and 93.46 percent higher than the first-order formulated models for the reduced and full integration models, respectively.

Table 2. Comparison of yielding results for all models.

Location	Variables	First-order reduced	First-order full	Second-order reduced	Second-order full
Tissue	Pressure, MPa (ksi)	15.3(2.22)	15.3(2.22)	11.6(1.68)	11.6(1.68)
	displacement, mm (in x 10^{-3})	0.2031(8.0)	0.2004(7.89)	0.1607(6.33)	0.1595(6.28)
Primary cartilage	Pressure, MPa (ksi)	20.3(2.94)	20.3(2.94)	16.6(2.41)	16.6(2.41)
	displacement, mm (in x 10^{-3})	0.3289(12.95)	0.3236(12.74)	0.2795(11.00)	0.2765(10.89)
Secondary cartilage	Pressure, MPa (ksi)	25 (3.63)	25 (3.63)	24.1 (3.06)	24.1 (3.06)
	Displacement, mm (in x 10^{-3})	0.6404(25.21)	0.6234(24.54)	0.9918(39.05)	0.9577(37.70)
Maximum Displacement, mm (in x 10^{-3})		0.6404(25.21)	0.6234(24.54)	1.2540(49.02)	1.206(47.48)

Figure 9. Comparison of maximum displacement of each FEM.

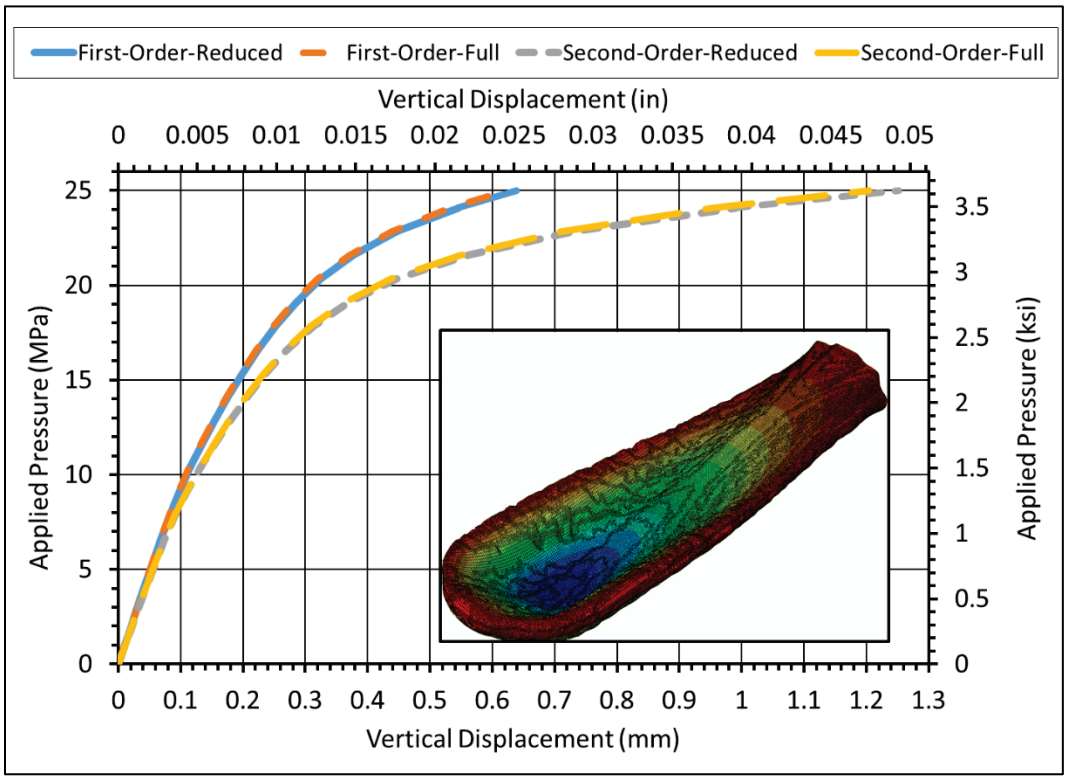

Figures 10 and 11 show a comparison of contour plots of von Mises stresses at the three loading stages based on values given in Table 2 for the first-order and second-order models with reduced and full integration. As mentioned before, the gray color is set once the stresses reach yielding. This comparison aids to appreciate the stiffening effect that has the formulation order in the overall model behavior. It shows that the second-order formulation model reaches similar yielding level at a lower applied pressure when compared with the first-order formulation model. This indicates that second-order formulated models possess lower stiffness

than the first-order formulation models. At maximum load, the second-order formulated model shows that most of the flat part of the rostrum has yielded while the first-order formulation model shows yielding concentrations in the thinner regions of the rostrum. Section thickness is appreciated in the section cuts shown in Figure 15a.

Figure 10. Comparison of contour plots of von Mises stresses for two of the models: \first-order-reduced integration (a, b, c), and second-order-reduced integration (d, e, f). Yielding regions are depicted in gray.

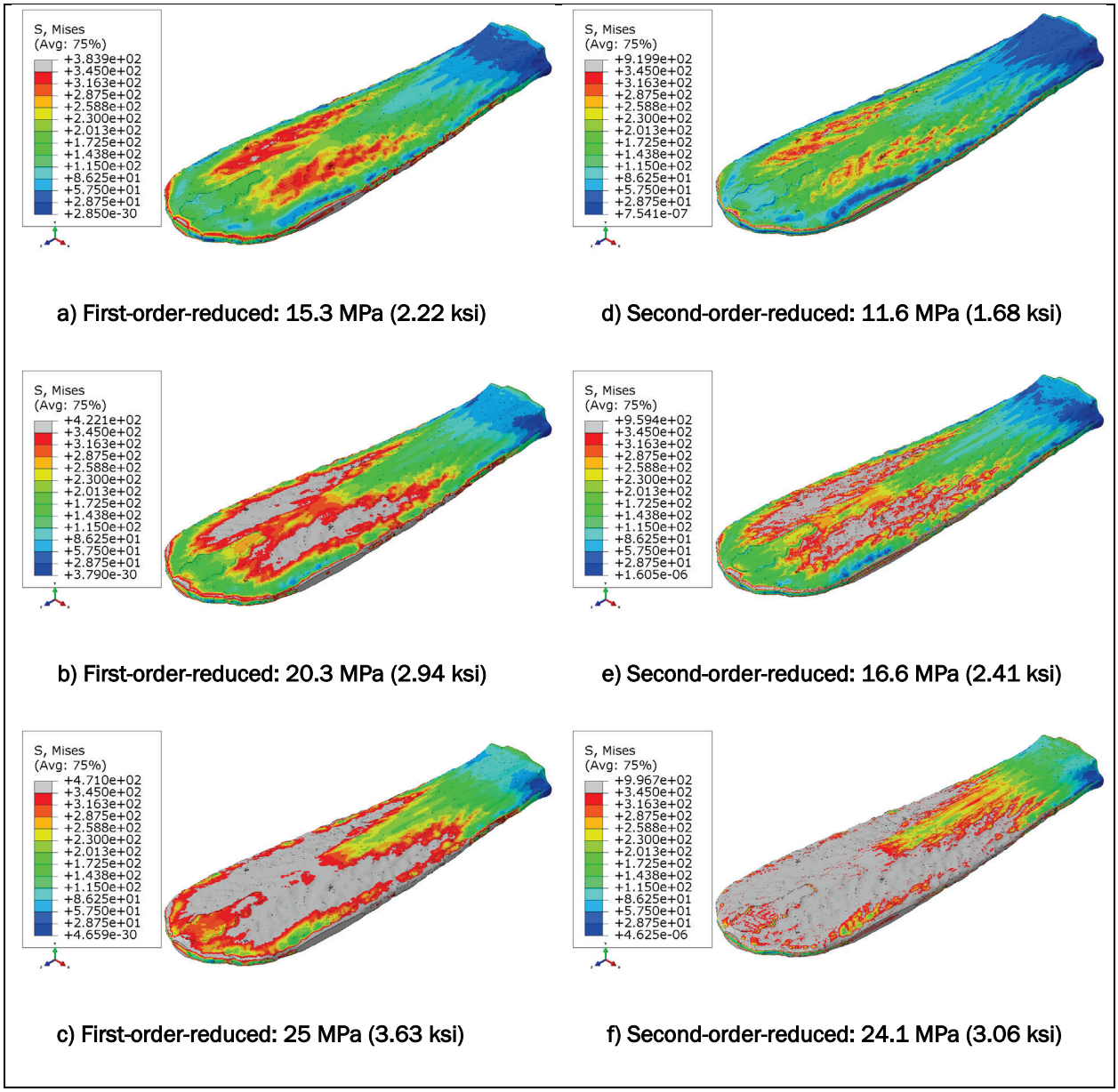

Figure 11. Comparison of contour plots of von Mises stresses for two of the models: first-order-full integration (a, c, e) and second-order-full integration (b, d, f). Yielding regions are depicted in gray.

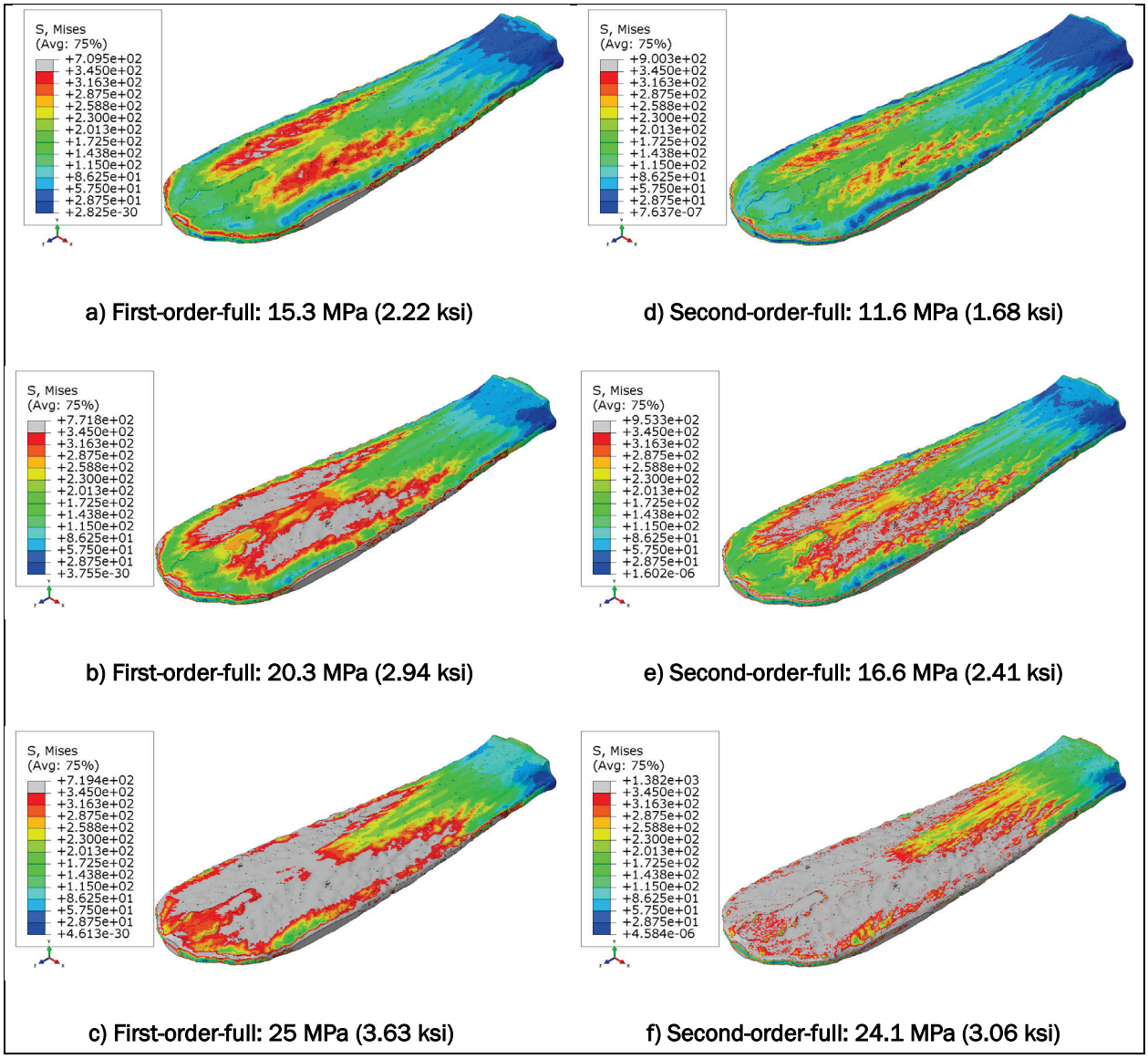

Figure 12 shows comparison of von Mises, σ_Z (z-axis), and σ_X (x-axis) stresses through the thickness of the rostrum at the two locations shown in Figure 13 (center path and point A path) for the four studied models. Figure 12 (a), (b), and (c) are for the center path and Figure 12 (d), (e), and (f) are for point A path. The sets of stresses are compared at two load levels: 6.6 MPa (0.96 ksi) – elastic range, and 25 MPa (3.63 ksi) – elastic-plastic range. The legend in the figures show the load level and the model name as LR for "Linear (first-order) Reduced integration," LF for "Linear (first-order) Full integration," QR for "Quadratic (second-order) Reduced Integration," and QF for "Quadratic (second-order) Full Integration." The figures also show reference location of the tissue, primary and secondary

cartilages. In addition, it shows the location of the centroid (half the thickness) and the approximate location of the neutral axis. Similar to the conclusions driven from Figure 9 comparing maximum displacements, in terms of stresses the four models provide similar behavior in the elastic range. However, once the geometrical nonlinearity and material plasticity start to occur, second-order formulation models exhibited higher stresses than models formulated with the first-order elements. The difference between full and reduced integration schemes are minimum.

In Figure 12a, for the von Mises stresses, results of the second-order formulated models have doubled near the neutral axis and in average, the stresses have increased about 31 percent. Stresses along the z-axis (Figure 12b) show higher differences between first-order and second-order formulated models at the maximum applied pressure than for the stresses along the x-axis (Figure 12c). The average increase in stresses along the x-axis is about 13 percent with values up to 27 percent, while for the z-axis is about 33 percent with values up to 64 percent. These graphs show that stresses along the z-axis are dominating the von Mises stresses.

In Figure 12d, for the von Mises stresses, results of the second-order formulated models have decreased more than 130 percent from the first-order to second-order model near the neutral axis, but it has increased up to 65 percent at other locations through the system. Stresses along the z-axis (Figure 12e) and x-axis (Figure 12f) show higher differences between first-order and second-order formulated models at the maximum applied pressure. These differences occurred near the neutral surface and in the tension side of the section. The maximum differences are 300 percent and 270 percent increase along the x-axis and the z-axis, respectively. Other values are 90 percent for the x-axis and 84 percent for the z-axis.

Results between the reduced and full integrations show similar results since the models are 92 percent tetrahedron elements that are formulated with full integration only. However, there are advantages of reduction of execution time and output file size when reduced integration formulation is used. In terms of mechanical behavior, there is a marked difference between first- and second-order element formulations, where the models show to be less stiff once the material starts to enter the plastic regime. It is also known that second-order formulation produce more accurate results than first-order formulated elements. Therefore, it is concluded that the model with second-order-reduced integration element formulation is to be used for future models. From this point, forward detailed discussions on stress distributions are focused on the second-order-reduced integration model.

Figure 12. Comparison of stresses (von Mises, σ_Z, σ_X) along paths through the thickness for the four models (Reference Figure 13).

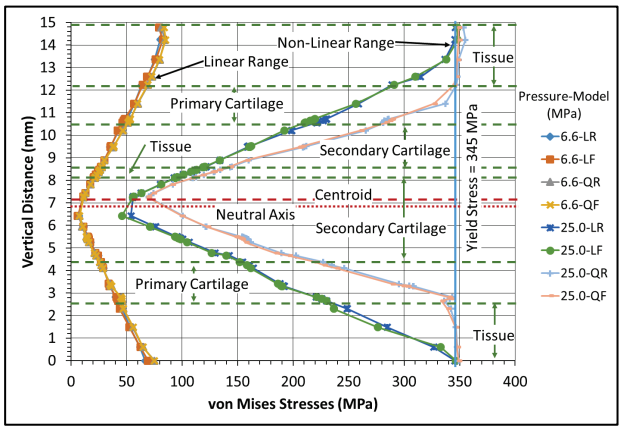

(a) von Mises at center path

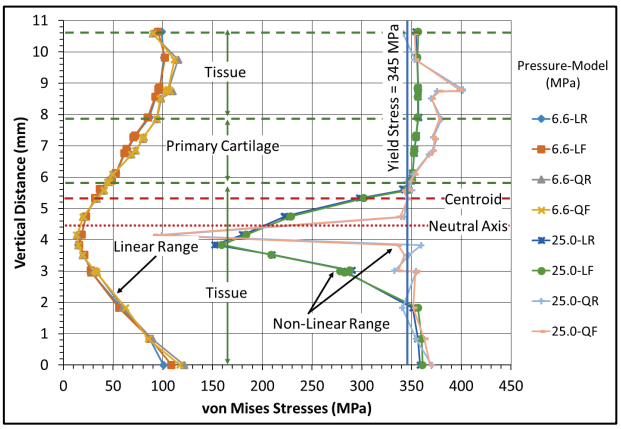

(d) von Mises at point A path

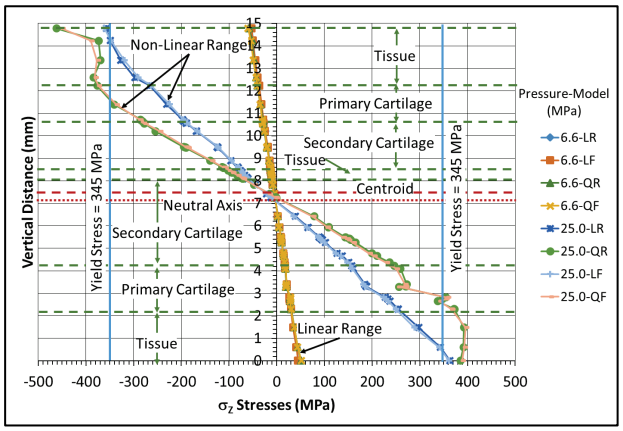

(b) σ_Z at center path

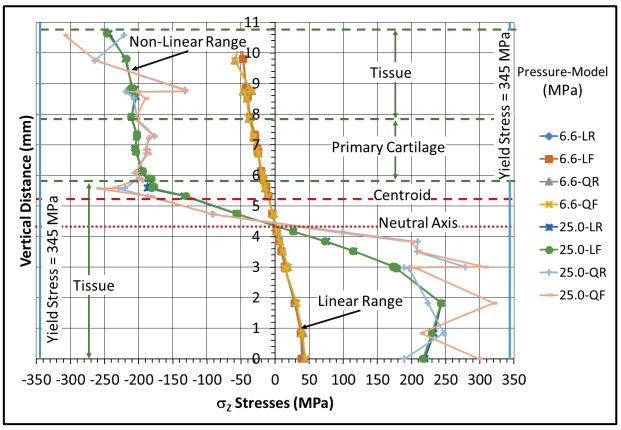

(e) σ_Z at point A path

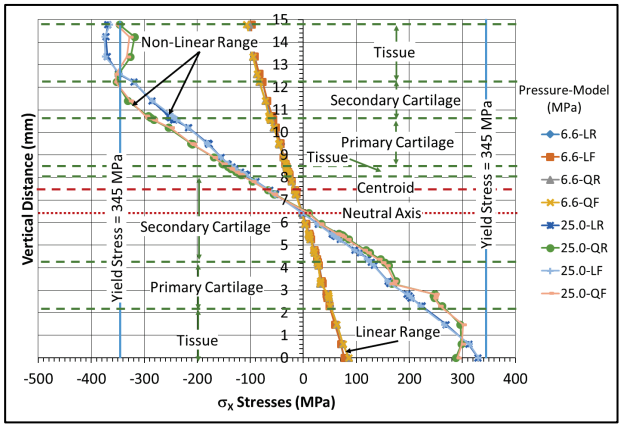

(c) σ_X at center path

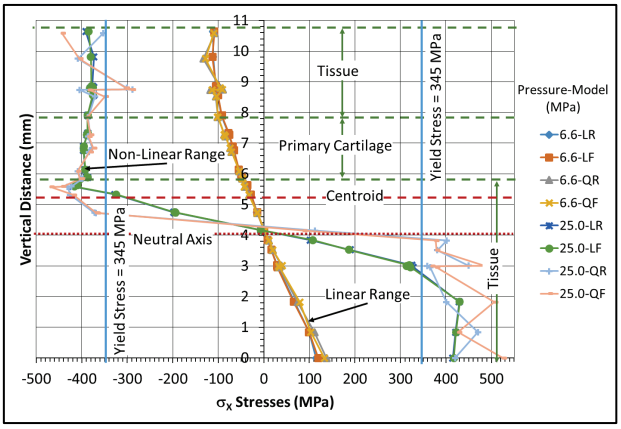

(f) σ_X at point A path

Figure 13. Reference location of two paths through the thickness at center and Point A (23 mm from the edge).

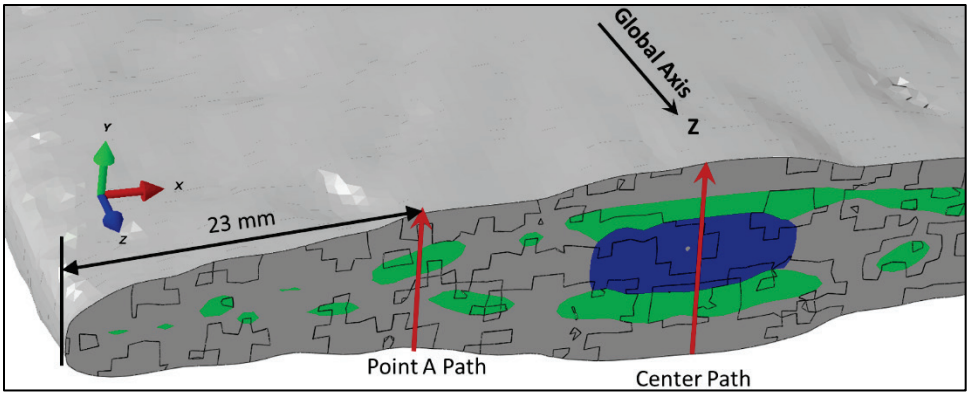

3.2 Global stresses

As stated earlier, the discussion of the results will focus only on the stress distributions on the second-order-reduced integration model. Paths along different rostrum directions and locations were created to extract the von Mises stresses. The path directions are shown in Figure 14. Plots of the actual paths are illustrated in Figure 15, where each part of the rostrum is highlighted in a different color. The horizontal paths were located on the top and bottom surfaces and one along the middle of the section. The surface paths on the top and bottom surfaces do not follow a straight line because they were generated following element edges that do not necessarily parallel to the principal coordinate axes. Mid-section paths were approximately located along the middle surface. Path A passes near the location of maximum displacement and stresses. Path B passes along the longitudinal central portion and path C is approximately 20 mm away from path B. von Mises stresses were extracted from the model as a function of the true distance along the paths. Their values are useful when a defined principal material and loading direction is not well defined. Their values may show yield while individual stress components may be below yielding.

Figure 14. Location of paths define to extract stresses (A – Location of maximum displacement, B – Center longitudinal direction, and C – Off center longitudinal direction).

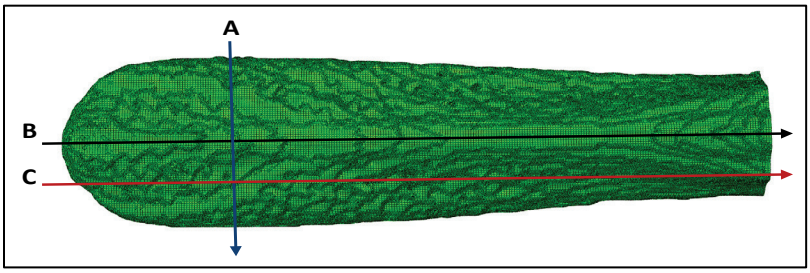

Figure 15. Location of path (red marks) in the actual rostrum model at (a) cross section, and (b) longitudinal section at the three locations (top and bottom surfaces and middle section).

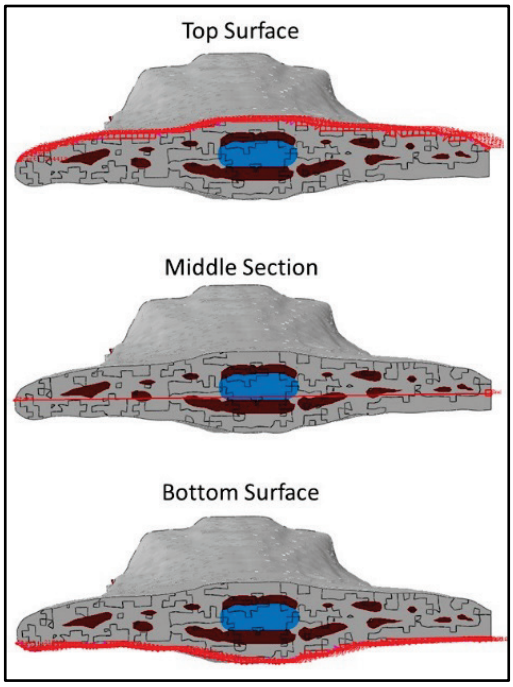

(a)

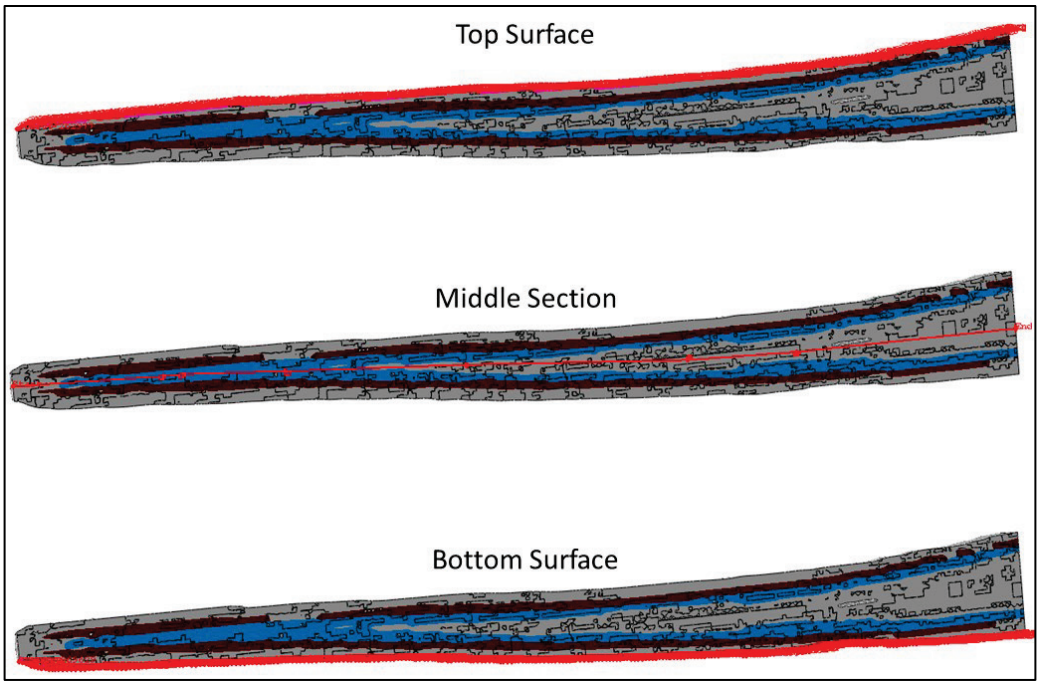

(b)

The following set of graphs (Figure 16, Figure 19, and Figure 22) report the von Mises stresses along the defined paths of the rostrum shown in Figures 14 and 15 of the second-order-reduced integration element formulation. The stresses are produced by three levels of applied pressures based on the yielding starting point of each rostrum component (shown in Table 2). Corresponding figures (a) are at 11.6 MPa (1.68 ksi), figures (b) are at 16.6 MPa (2.41 ksi), and figures (c) are at 24.1 MPa (3.50 ksi) where the values at the top surface are red, at the center are gray, and at the bottom are green. For reference purpose, the yield stress value (345 MPa) is highlighted in the graphs. The true behavior of the rostrum on the fish is as a cantilever tapered beam. However, this analyses applies boundary conditions that simulate fixed end conditions around the edges similar to plate behavior for better correlation. This boundary condition changes the rostrum mechanics, and it can be seen in the plots.

Figure 16. von Mises stresses for second-order-reduced integration model along the horizontal cross-section paths at the load levels (a, b and c) that each component starts yielding.

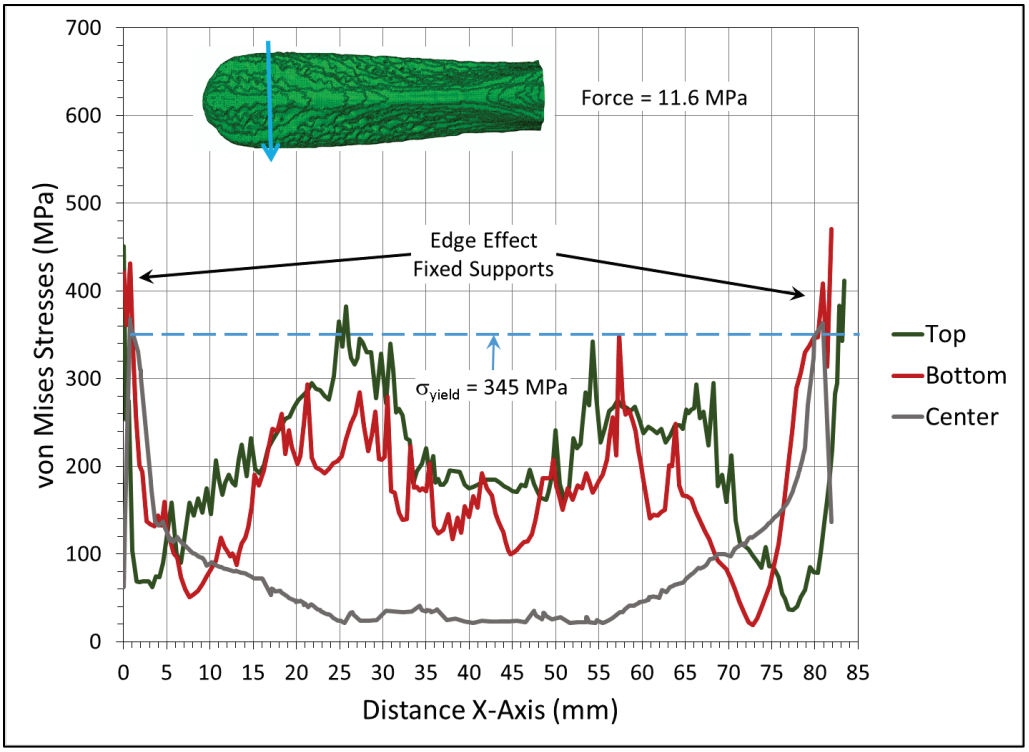

(a)

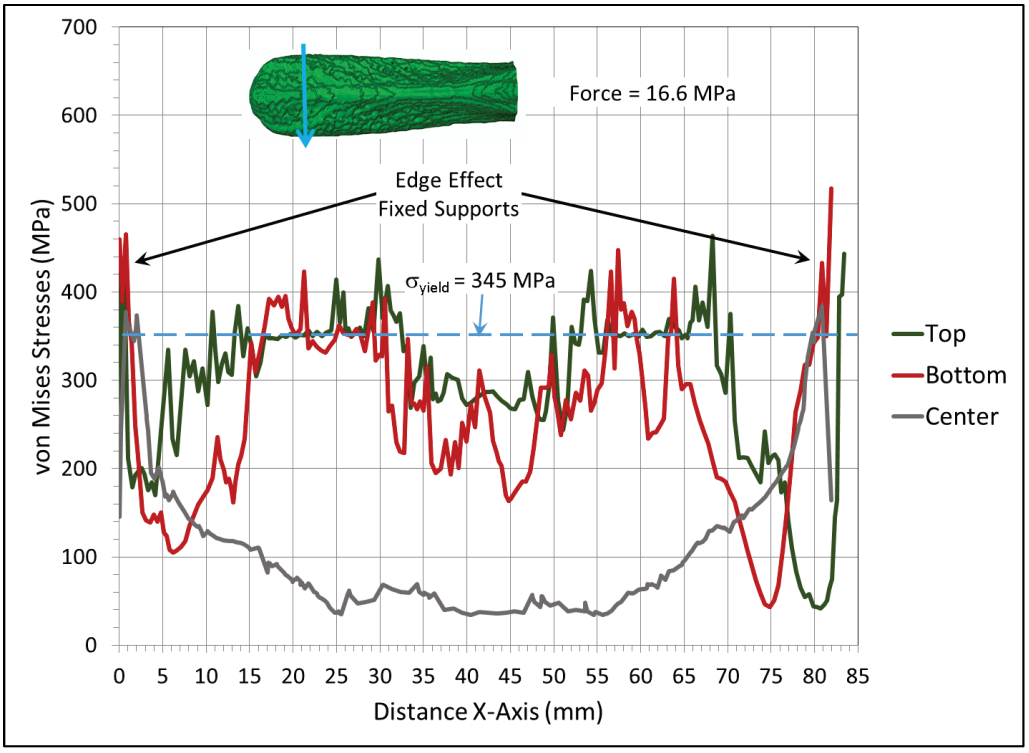
Force = 16.6 MPa
Edge Effect
Fixed Supports
σyield = 345 MPa
von Mises Stresses (MPa)
Distance X-Axis (mm)
Top
Bottom
Center

(b)

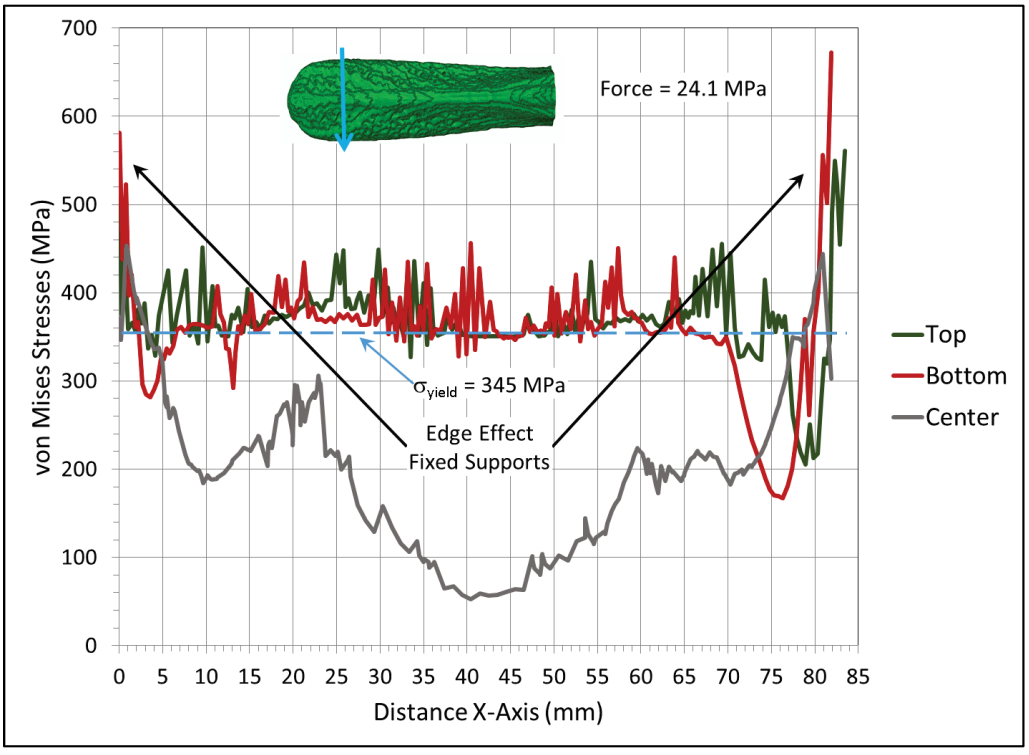
Force = 24.1 MPa
σyield = 345 MPa
Edge Effect
Fixed Supports
von Mises Stresses (MPa)
Distance X-Axis (mm)
Top
Bottom
Center

(c)

Before discussion of the stress plots, it must be pointed out that the lack of smoothness in the resulted stress variations observed in the following set of graphs can be attributed to the way the paths were defined and the element generated. Paths were defined in some instances by element edges that did not necessarily follow a straight line. ABAQUS calculates stresses at the nodes near or intersected by the path, and average nearby elements depending on the path definition. The user has little control on how the values are calculated, thus generating curves that may not necessarily result in a smooth variation.

Figure 16 reports the von Mises stresses along the path direction A (width of the rostrum) at the three applied pressures. The graphs show an increase in stresses at the edges of the rostrum where fixed supports are located. This is an edge effect caused by the multiple pinned nodes in the region to produce the fixed-end condition. As it moves to the center from the edges of the rostrum, top and bottom stresses are increasing, but at the center path the stresses are low. Low stresses at the center are expected since this path is close to the neutral axis. The rostrum is stiff at the center because this is the location of the center bone, which is stiffer due to the higher separation that exists between the two parts of the bone. The moment of inertia is larger, resulting in higher flexural stiffness. The section is much thinner as the edges, acting similar to a thick shell, with both flexural and membrane actions. Towards the center it behaves similar to a plate. From the stresses it can also be observed that the rostrum is fairly symmetric along the z-axis. However, as the load is increased, the stress distribution starts to lose its symmetry. Figure 17 shows stresses along the x-axis (local stresses) at the top, bottom and center paths at the load level that the tissue starts to yield. It is noticed that two inflection points are visible at the location where the top and bottom stresses cross. This happens about 5 mm from each edge of the rostrum. Similar to the von Mises stresses shown in Figure 16, lower stresses occur at the center of the rostrum where the thickness of the section is higher. The vertical displacements of the central paths shown in Figure 18 reveal interesting facts about the rostrum. The displacement curves at the stress levels where low yielding has occurred show to be symmetric with respect to the center of the rostrum. Also the graph shows a plateau along the width of the central bone where the section is stiffer. However, at an applied load of 24.1 MPa (3.06 ksi), where the section is experiencing high amount of yielding, the displacements are not symmetric, with a larger displacement at the location that corresponds to the highest von Mises stresses shown in Figure 16 c. This phenomenon could be attributed to a slight unsymmetry of the model and the technique used for the mesh generation, and the boundary conditions.

Figure 17. Stresses along the x-axis for the second-order-reduced integration model along the horizontal section paths at a load of 11.6 MPa (tissue starts to yield).

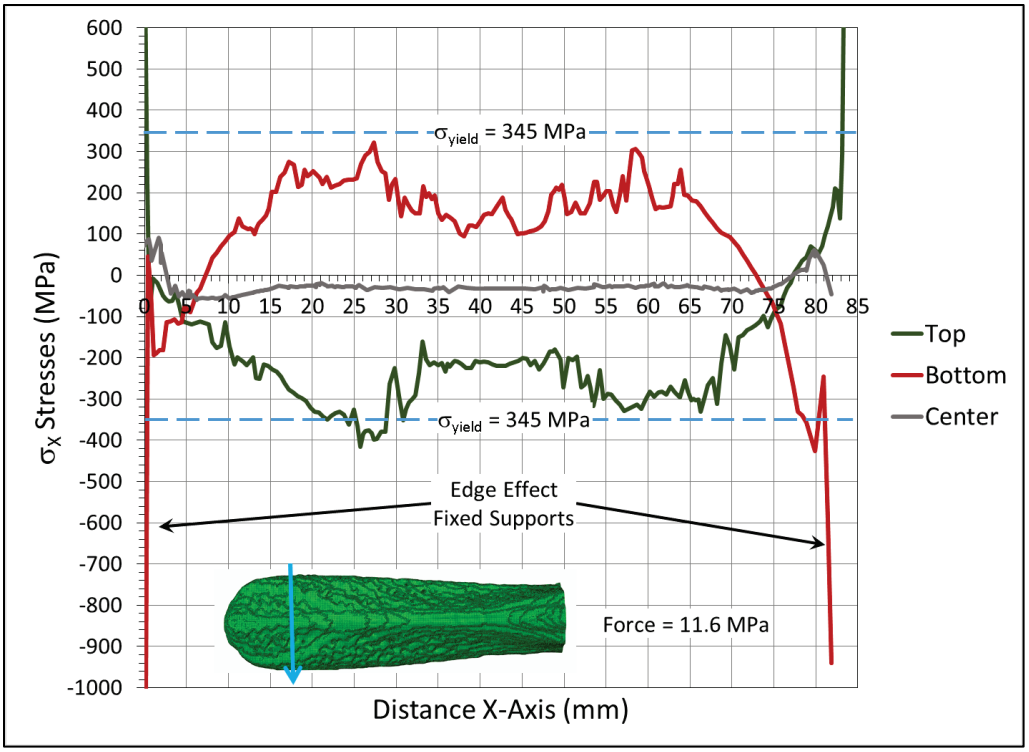

Figure 18. Vertical displacement for the internal path along the x-axis at the three load levels where each component starts to yield.

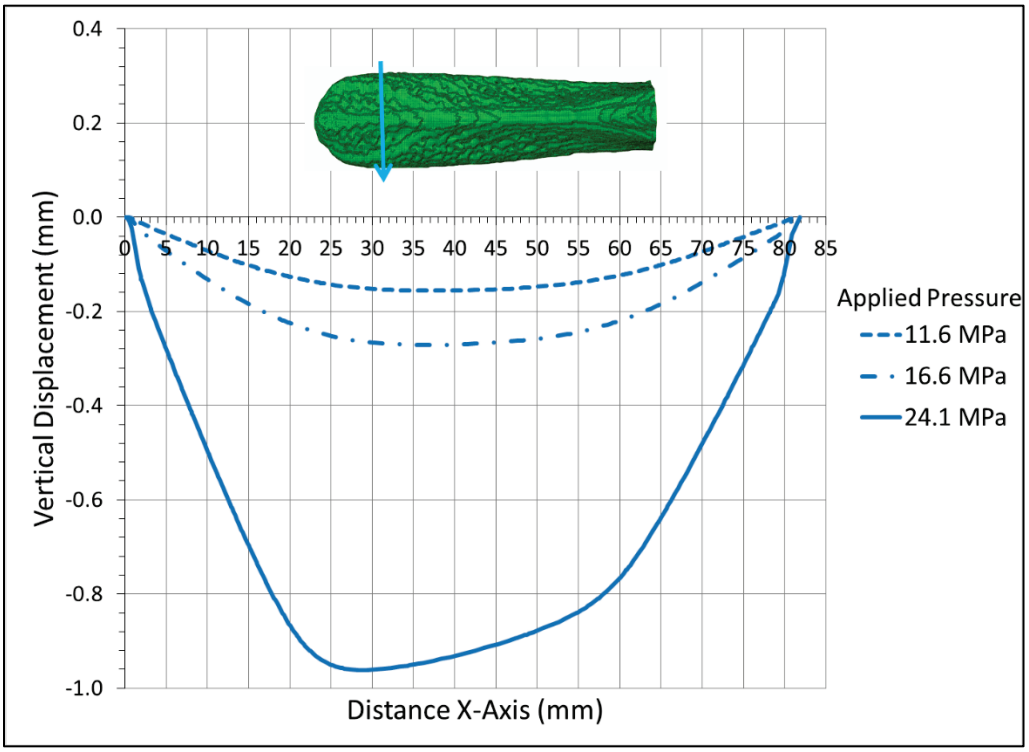

Stress plots along the longitudinal axis (Figure 19 and Figure 22) show that the rostrum is stiff towards the mouth end (narrower and thicker section) as their values are lower than at the thinner but wider end. Stresses along the center of the rostrum (Figure 19) remain below yielding during most of the analysis until the applied pressure reached 24.1 MPa (3.06 ksi). Stress increase due to boundary conditions are also observed. Figure 19c shows that stresses are at yielding at a distance to about 115 mm. Then the values drop below yielding reaching minimum value at a distance between 135 to 140 mm. Then the stresses increase again to a peak at 200 mm. Stresses along the z-axis are shown in Figure 20 at the same applied load as the stresses in Figure 19c. The stresses drop at the previously mentioned location because at this zone is an inflection point where the stress signs reverse. von Mises stresses do not reach a lower value because there are stresses at the other two planes acting along the same path. Figure 20 shows the vertical displacement for the central path along the z-axis at the three applied load levels. The approximate location of the inflection points is marked in the figure. Notice that the increase in displacement is about double (111 percent) from the applied load of 11.6 MPa to 16.6 MPa. However, the displacement has a dramatic increase of near three times (270 percent increase) when the load increased from 16.6 MPa to 24.1 MPa. At this point most of the section is experiencing yielding. In Figure 22 at the location away from the center, stresses are quickly reaching yielding. In all curves, a rapid increase in stresses near the center of the rostrum is observed as it reaches the supports, implying a tensile dominated behavior. Figure 23 shows the displacements along the central path that correspond to the off-center of the rostrum (path C). Similar behavior as from displacements of Figure 20 is observed here.

Figure 19. von Mises stresses for second-order-reduced integration model along the horizontal longitudinal center section paths at load levels (a, b and c) that each component starts yielding.

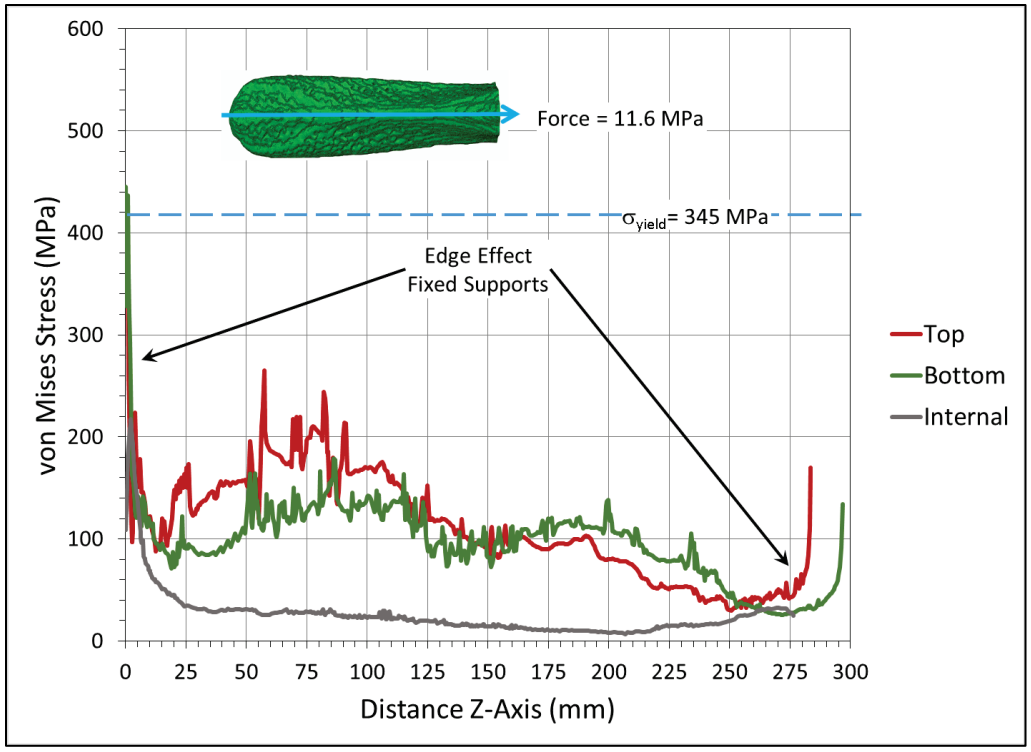

(a)

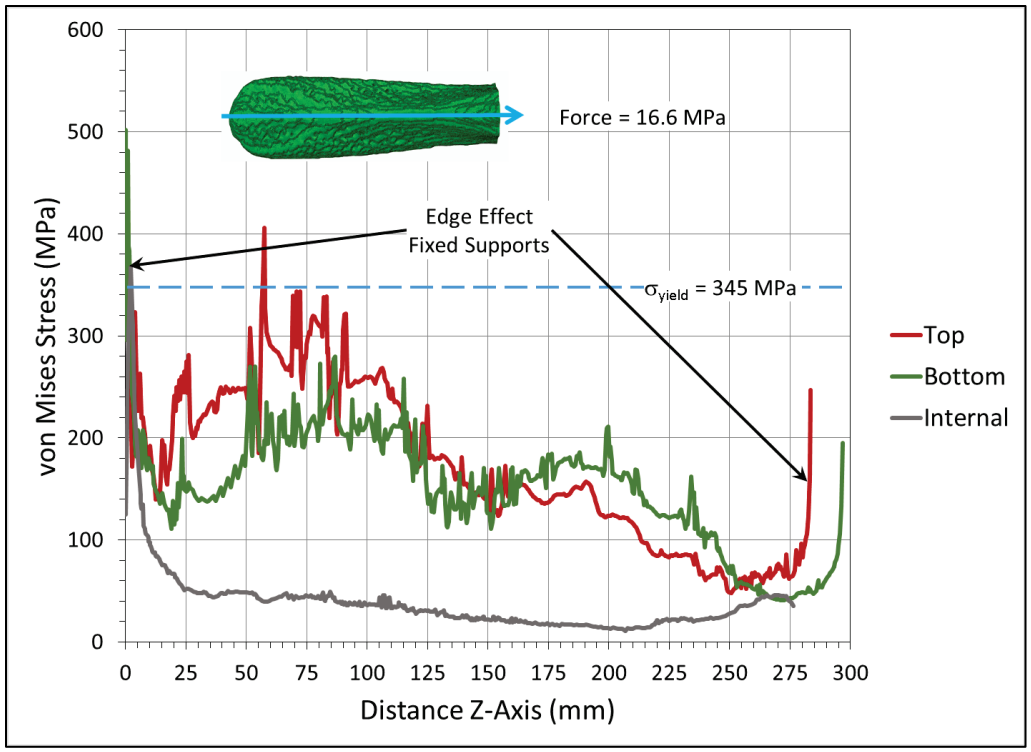

(b)

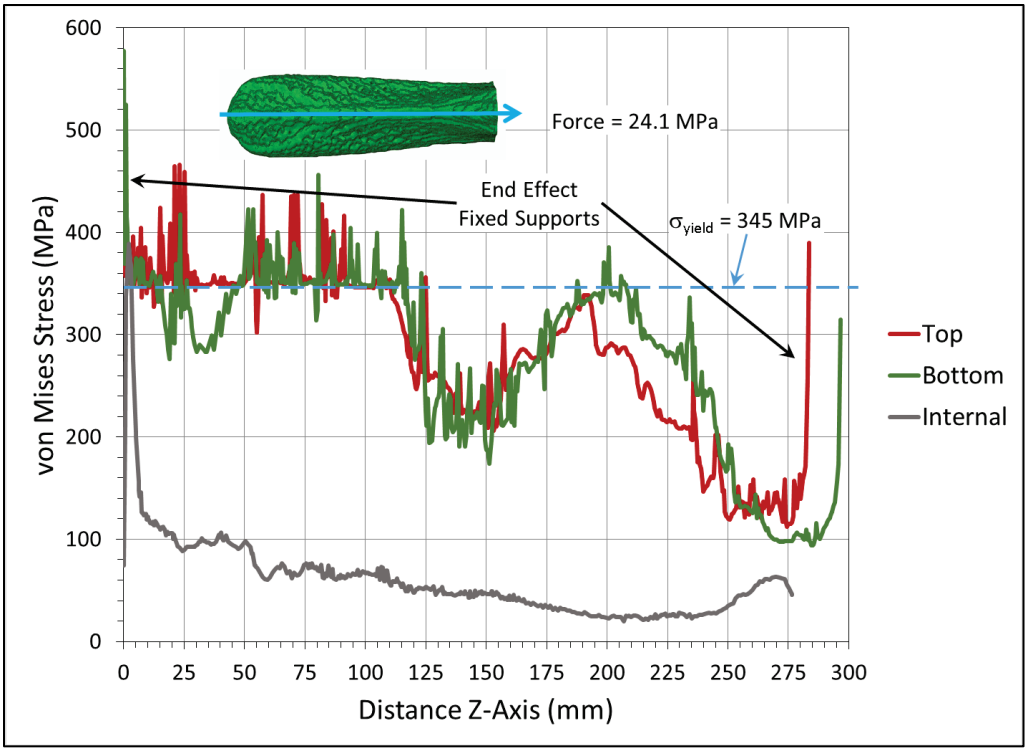

(c)

Figure 20. Longitudinal (σ_Z) stresses for second-order-reduced integration model along the horizontal longitudinal center section paths at level of yielding of the secondary cartilage (24.1 MPa).

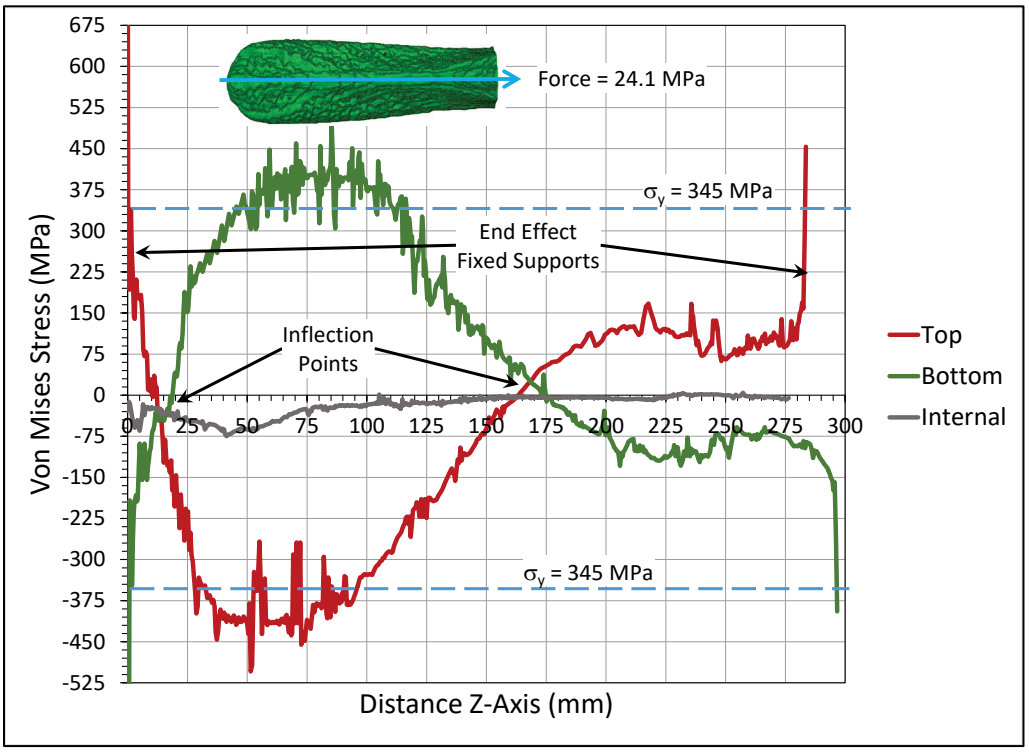

Figure 21. Vertical displacement for the internal path along the z-axis, center, at the three load levels where each component starts to yield.

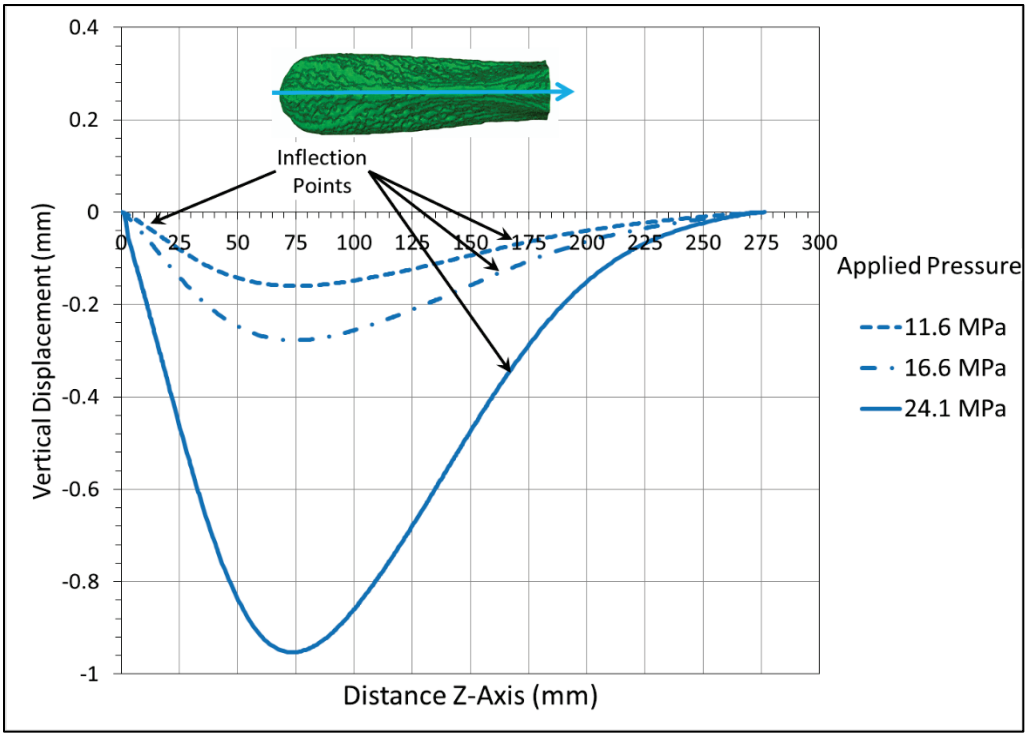

Figure 22. von Mises stresses for second-order-reduced integration model along the horizontal longitudinal off-center section paths at load levels (a, b and c) that each component starts yielding.

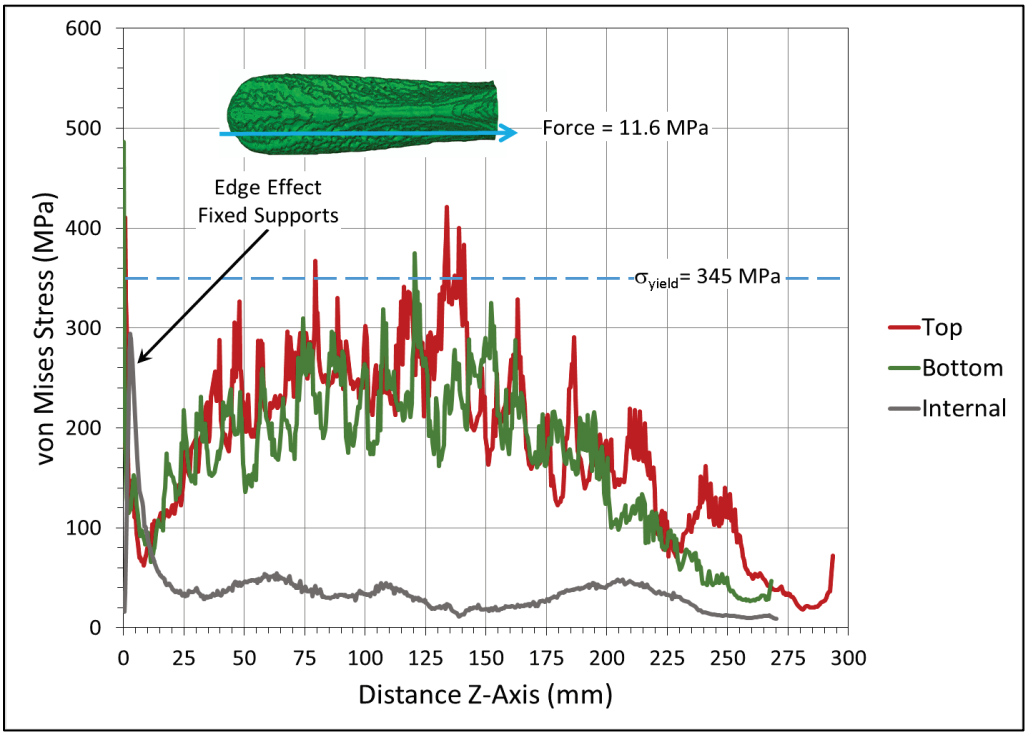

(a)

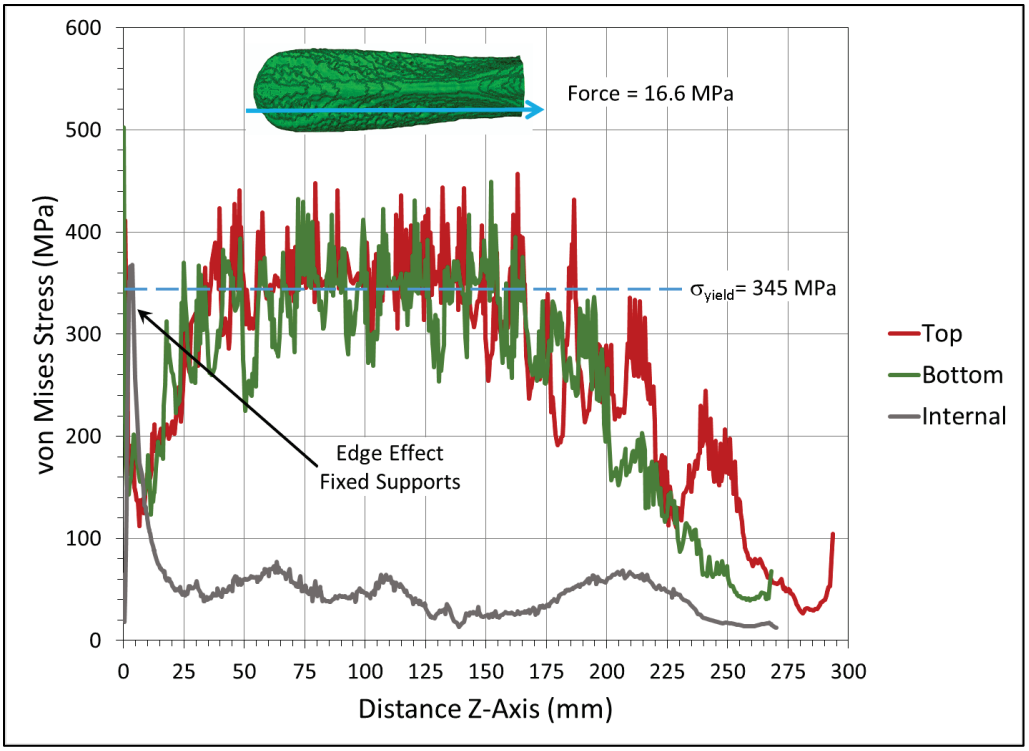
Force = 16.6 MPa
σyield= 345 MPa
Edge Effect
Fixed Supports
Top
Bottom
Internal
von Mises Stress (MPa)
Distance Z-Axis (mm)
0
100
200
300
400
500
600
0 25 50 75 100 125 150 175 200 225 250 275 300

(b)

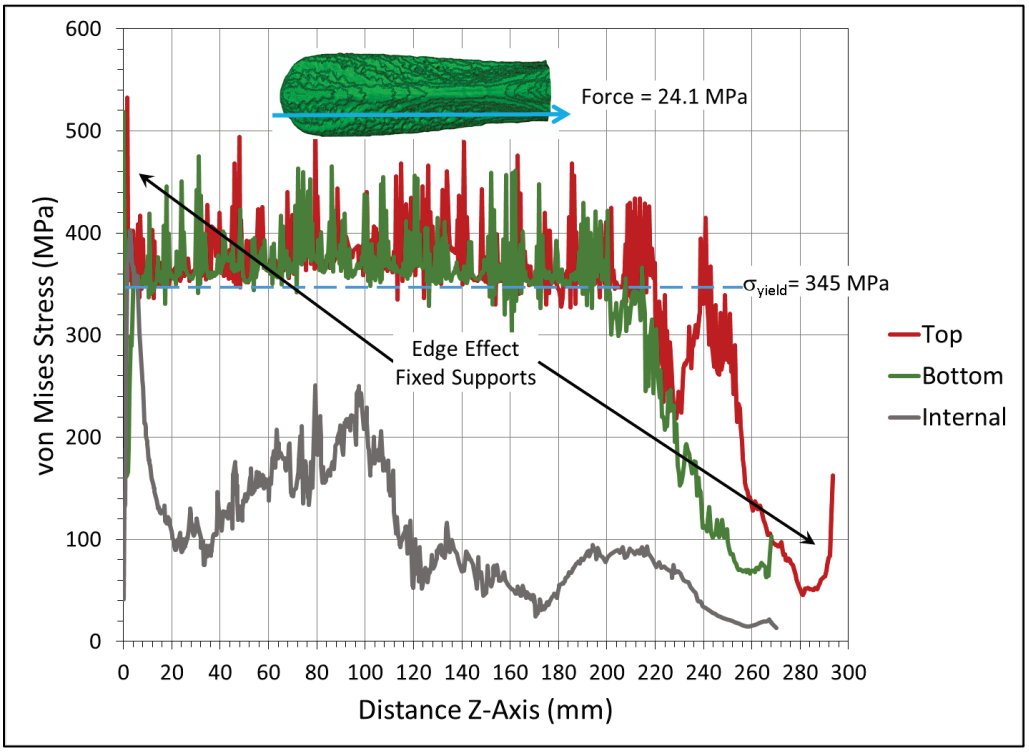
Force = 24.1 MPa
σyield= 345 MPa
Edge Effect
Fixed Supports
Top
Bottom
Internal
von Mises Stress (MPa)
Distance Z-Axis (mm)
0
100
200
300
400
500
600
0 20 40 60 80 100 120 140 160 180 200 220 240 260 280 300

(c)

Figure 23. Vertical displacement for the internal path along the z-axis, off-center, at the three load levels where each component starts to yield.

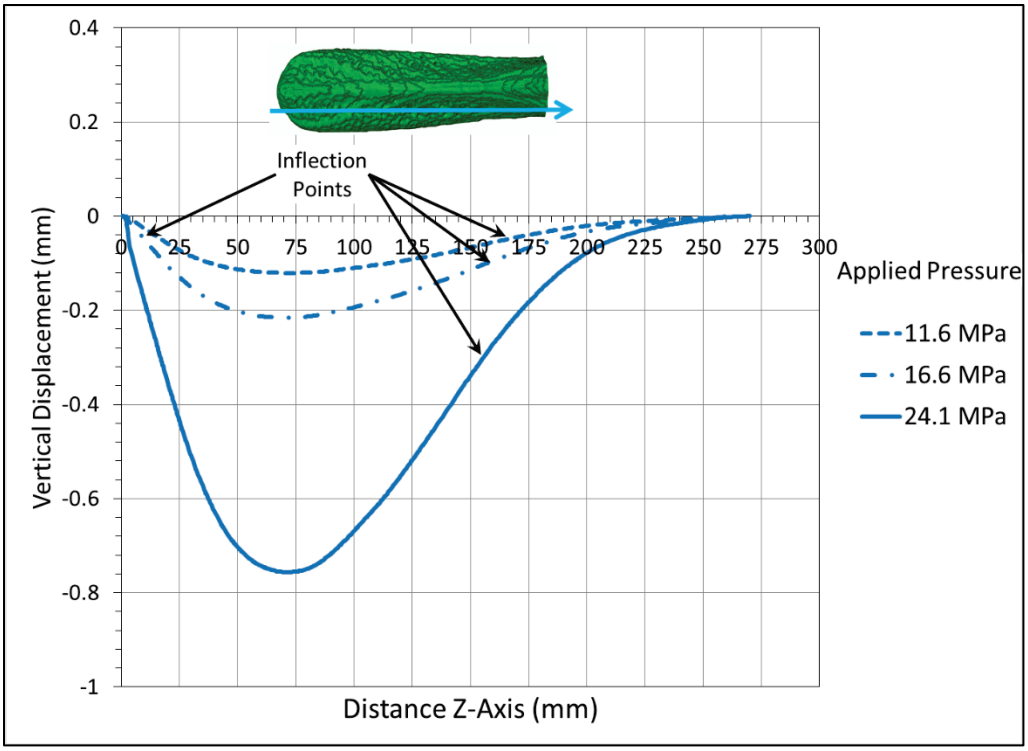

3.3 Yielding progress at primary cartilage

Figure 24 and Figure 25 show contour plots of the von Mises stresses at the primary cartilage zone at different load increments for second-order reduced and full integration models. Contour colors were limited up to the yield stress (345 MPa), so gray color means that values have reached and exceeded this value. The load increments of the plots are 1.83 MPa (0.27 ksi), 6.59 MPa (0.96 ksi), 14.09 MPa (2.04 ksi), 17.84 MPa (2.59 ksi), 20.34 MPa (2.95 ksi), 22.84 MPa (3.31 ksi), and 25.0 MPa (3.63 ksi). Similar to previous observations, the yielding zone is larger with the second-order models as opposed to the first-order models, regarding the integration order. Yielding also starts at a lower load level.

Figure 24. von Mises stresses contour plots at the primary cartilage section with respect to each selected load increments. Gray color means post yielding stress (Second-order-reduced integration).

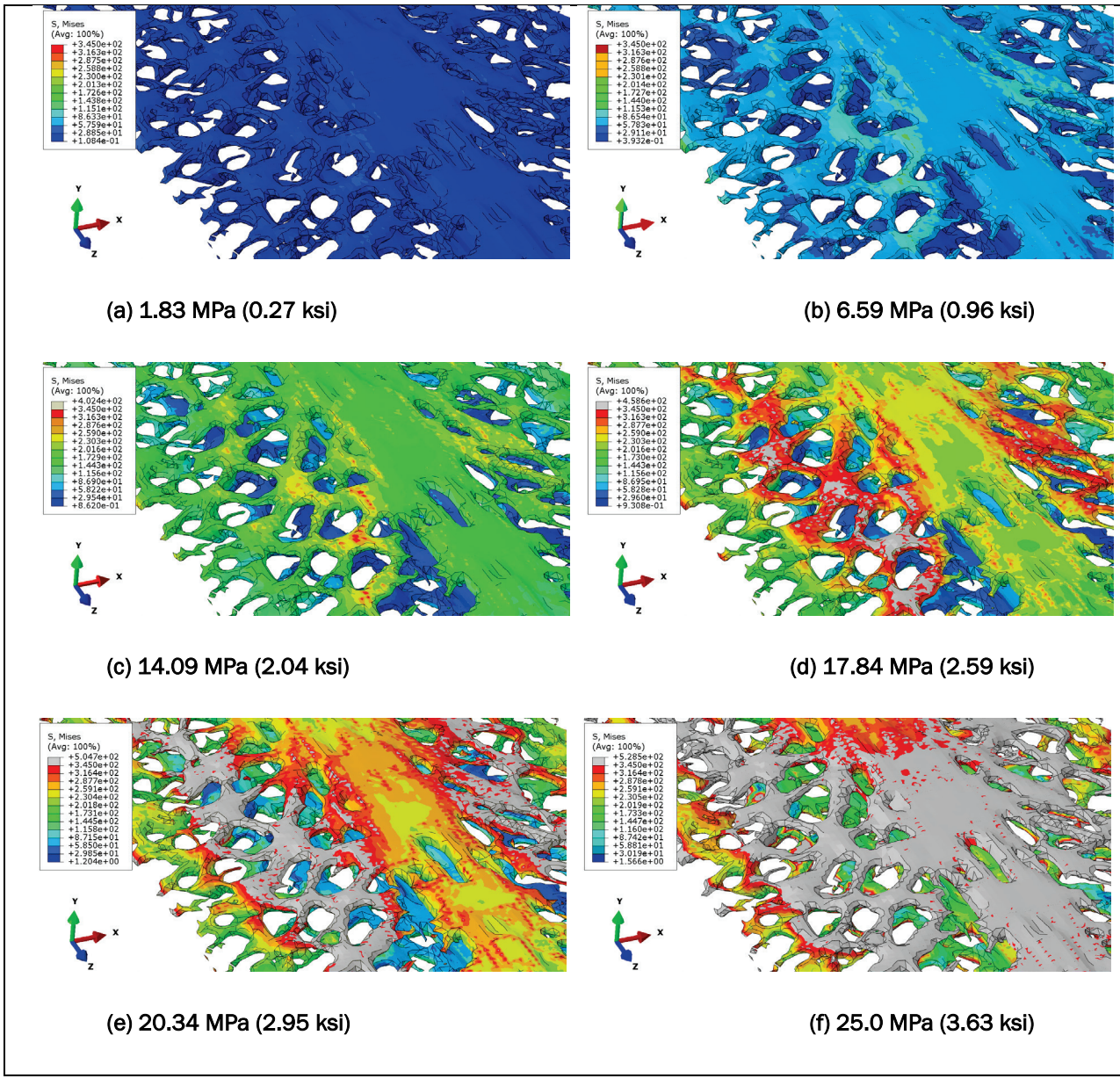

Figure 25. von Mises stresses contour plots at the primary cartilage section with respect to each selected load increments. Gray color means post yielding stress (Second-order-full integration).

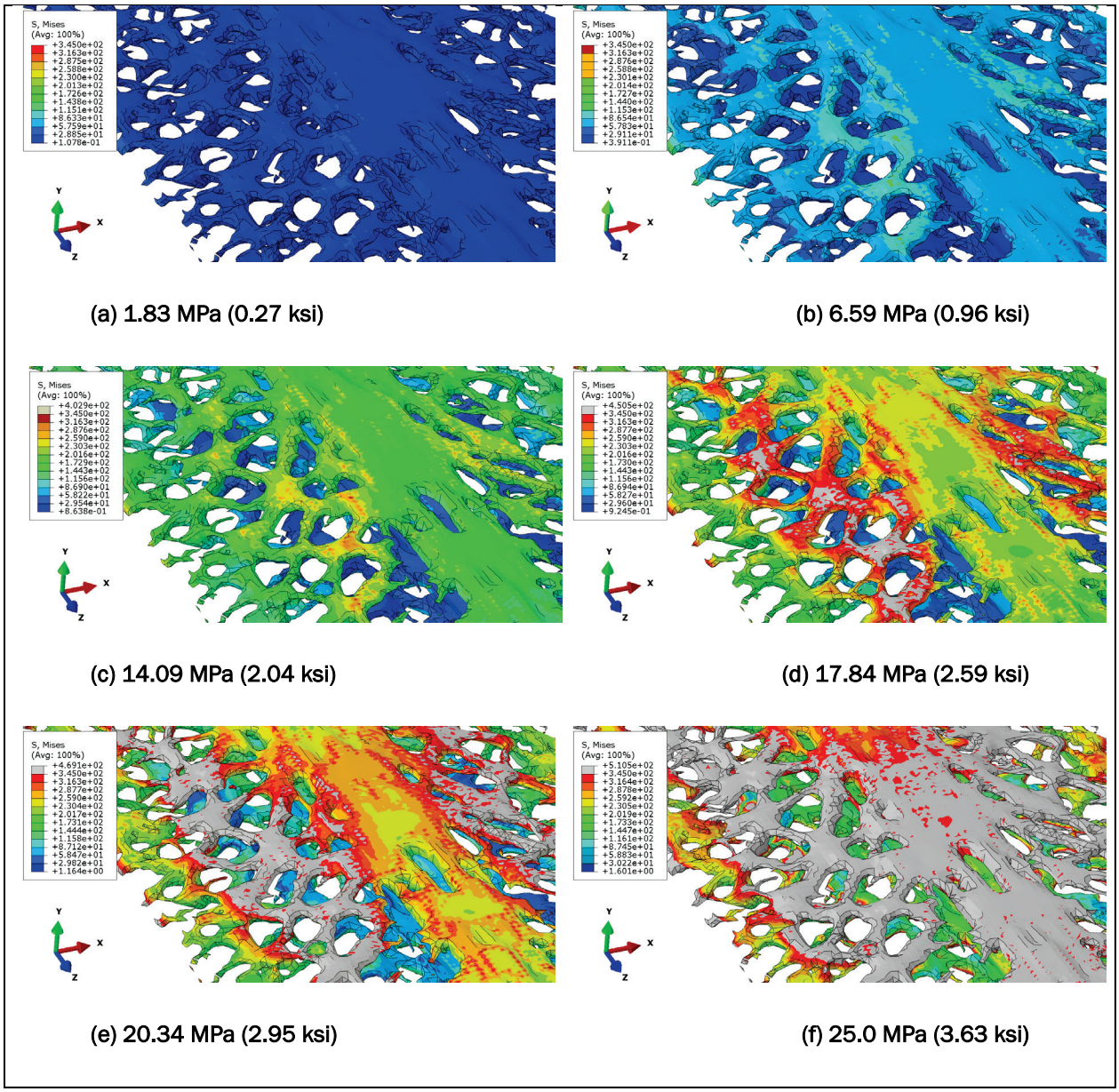

3.4 Stress distributions through thickness and cartilages

A zone at the flat part of the rostrum was selected to evaluate stress distributions through the thickness with respect to the applied pressure. Stresses evaluated include von Mises, σ_X (global x-axis), σ_Z (global z-axis) and σ'_X (local x-axis) where applicable. Vertical paths that cross each zone were defined and nodes in key locations were also selected. Also stresses were evaluated at the center of the rostrum where the three main rostrum components pass. References of these locations are shown in Figure 26 a, b,

and c, where only the primary cartilage is depicted in (a) and (b). Figure 26a includes the location of the cut used to evaluate stresses near the location of maximum displacement at the wider cross section of the rostrum. This cut line also passes through a cartilage joint (Point A) to study how the stresses are distributed through stellate cartilages. Stresses of these locations used the global reference axes shown in Figure 26a. 26a also shows the location of the group of cartilages to be evaluated. These cartilages named B through G, are connected at A. Stresses at these locations were evaluated using a local axis indicated in Figure 26b. The selected location is near the zone of maximum stress and displacement described in subsection 3.1. Most of the vertical paths crossed only one cartilage. However, paths through cartilages D, F, and G crossed also a bottom cartilage and allowed to find if there was an interaction between them. Results for the center cut and point A are discussed individually because their reference axes are the same, and they are located at important sections of the rostrum. Results for points B through G are grouped and discussed together to highlight the most notable characteristics of their behavior in comparison to each other.

3.4.1 Center of rostrum

Figure 27 presents a cut of the rostrum at the center where all three components are located (tissue - green, primary cartilage - red, and secondary cartilage - blue). The figure also shows the location of the vertical path used to extract stresses as a function of the vertical location through the thickness. This path starts at the bottom of the rostrum (y-axis) and ends at the top surface. The figure also shows the location of the nodes used to extract stresses as a function of applied pressure. The location of these nodes are close to the path, but they are not necessarily in it. These nodes are strategically picked to record stresses at key points. N-1 and N-14 are in the tissue. N-2 and N-13 are at the interface of tissue and primary cartilage. N-4 and N-11 are at the interface of primary and secondary cartilages. N-5 through N-10 are inside the secondary cartilage. Finally, N-3 and N-12 are inside the primary cartilage. At this location, the thickness of the rostrum is near 15 mm (0.60 in). The following plots of stresses provide a means to understand how the state of stresses varies through the different rostrum components.

Figure 26. Reference for global axes and local axes in primary cartilage: (a) transverse cut and cartilage labels, (b) reference local axes and cartilage labels, (c) through the thickness.

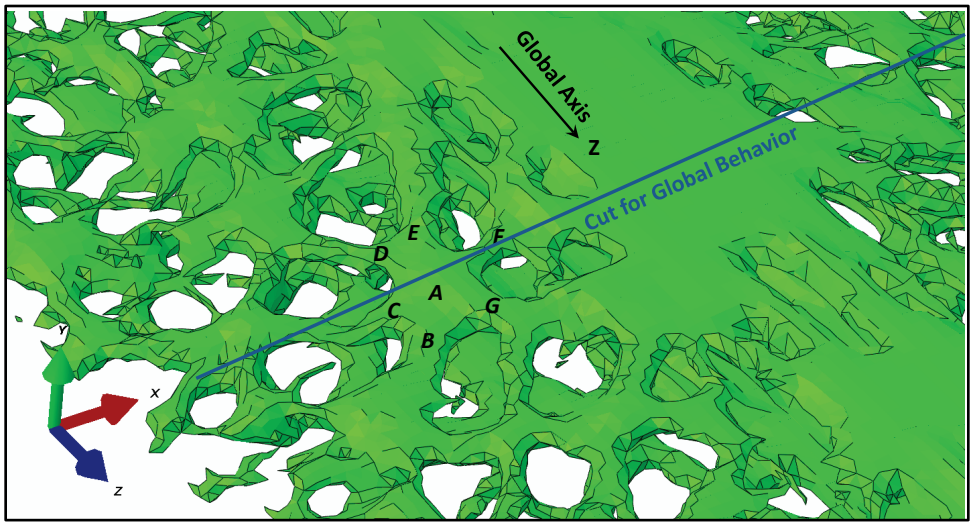

(a)

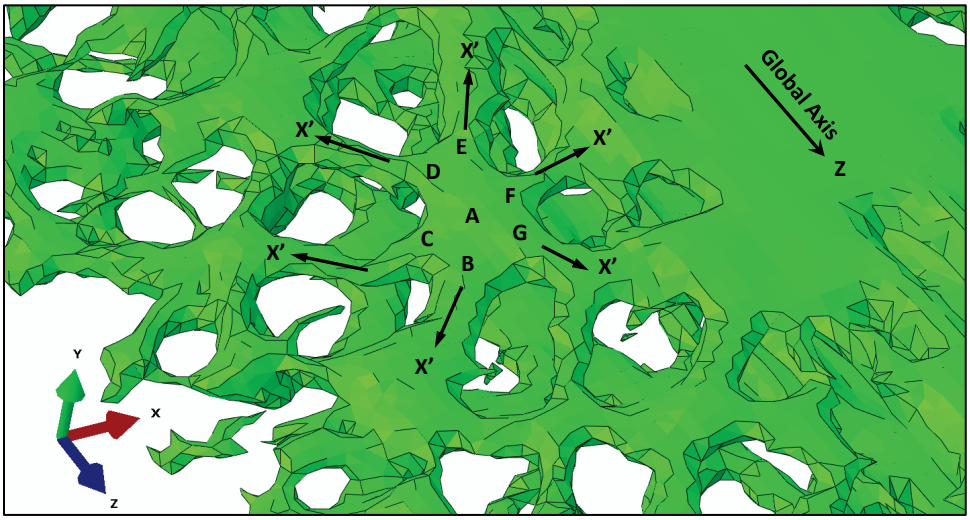

(b)

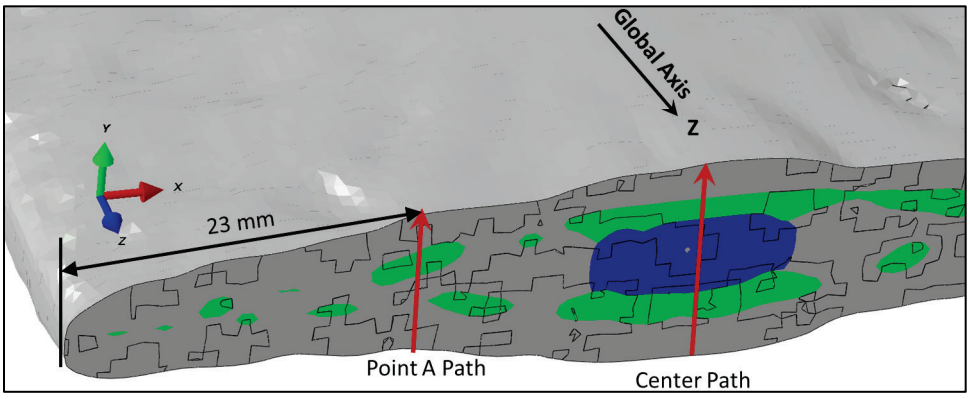

(c)

Figure 27. Illustration of the vertical path and node location for the center portion of the rostrum (green – tissue, red – primary cartilage, blue – secondary cartilage).

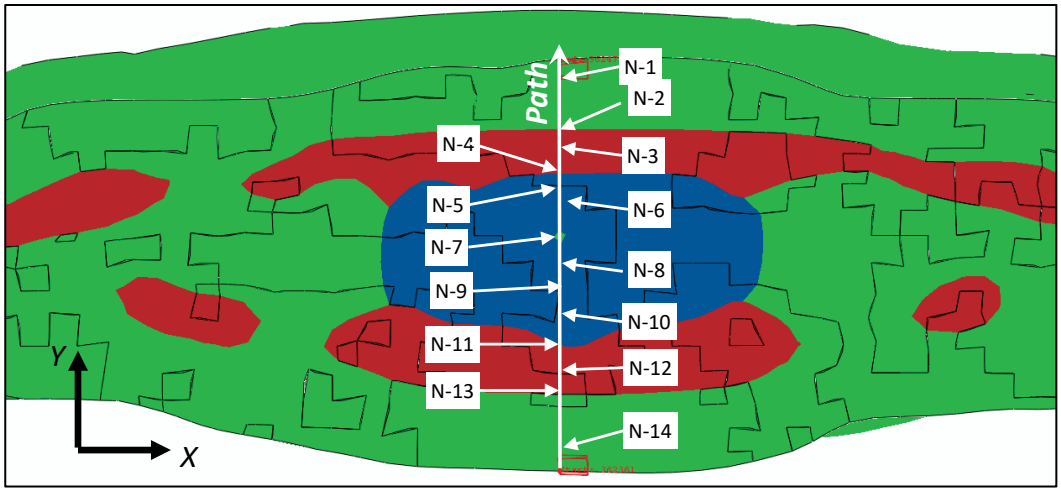

Figure 28 and Figure 29 (a) and (b) show von Mises, σ_x (global x-axis), and σ_z (global z-axis) stresses for the selected nodes through the thickness indicated in Figure 27. The stresses are varying as a function of the applied pressure. Yield stress is marked in each figure for reference purposes. Also the applied pressure at which yielding starts (elasto-plastic behavior) is indicated in each figure. Positive stresses in Figure 29 are from the nodes located below the centroid of the rostrum at the tension side and negative stresses are for nodes located above the centroid at the compression side. In Figure 28 it is observed that based on the von Mises stresses and the node location with respect to the section, N-1, N-2, N-13 and N-14 are experiencing stress values at yielding at applied pressures between 23 and 24 MPa, but N-2, N-13, and N-14 are reaching yielding at the maximum applied pressure of 25 MPa. As stresses reach and pass the yield point, their rate of change with distance is reduced dramatically with change in pressure. The figure also shows that N-3 and N-12 are just below yielding. It means that at the maximum applied pressure, the tissue and the primary cartilage regions are experiencing yielding. Figure 29 (a) (σ_Z) show that nodes N-1, N-2, N-3, N-13, and N-14 are at yielding. However, stresses along the x-axis in Figure 29 (b) (σ_X), only N-1 and N-2 are at yielding stresses. This means that what is dominating the yield surface is the stresses along the global z-axis or the longitudinal stresses, where the section is stiffer.

Figure 28. Variation of von Mises stresses at selected nodes with applied pressure at the center of the rostrum for the second-order-reduced integration model. (Reference in Figure 27).

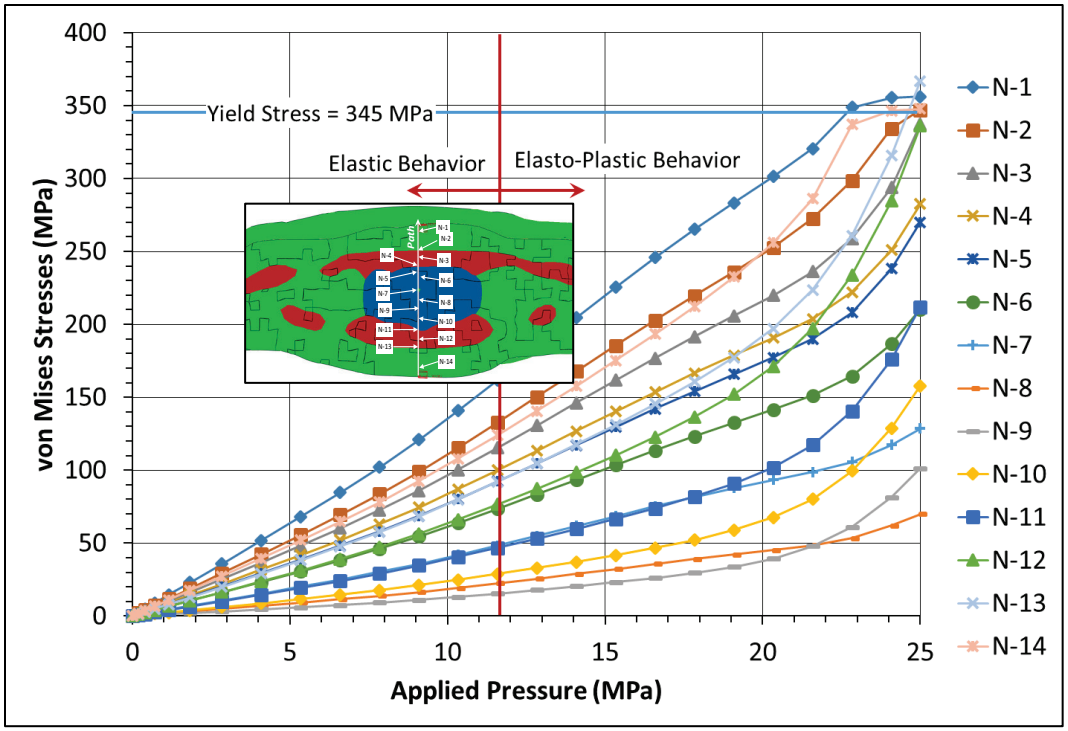

Figure 29. Variation of stresses (a) along the z- and (b) along the x-axes at selected nodes with applied pressure at the center of the rostrum for the second-order-reduced integration model. (Reference in Figure 27).

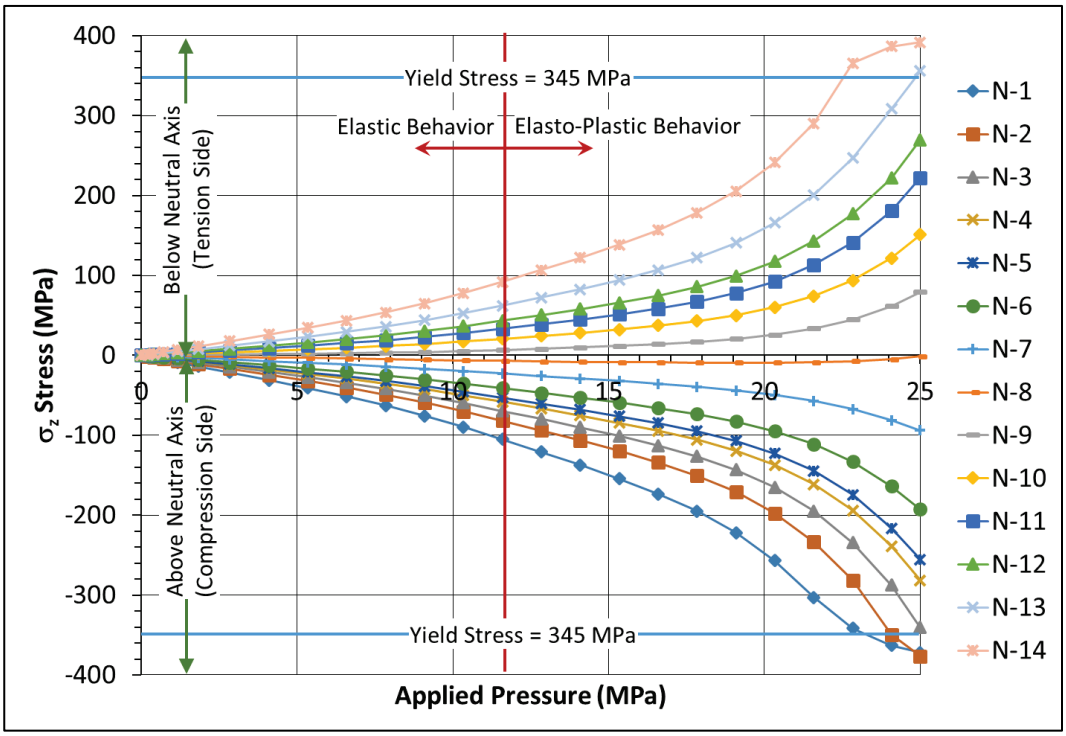

(a)

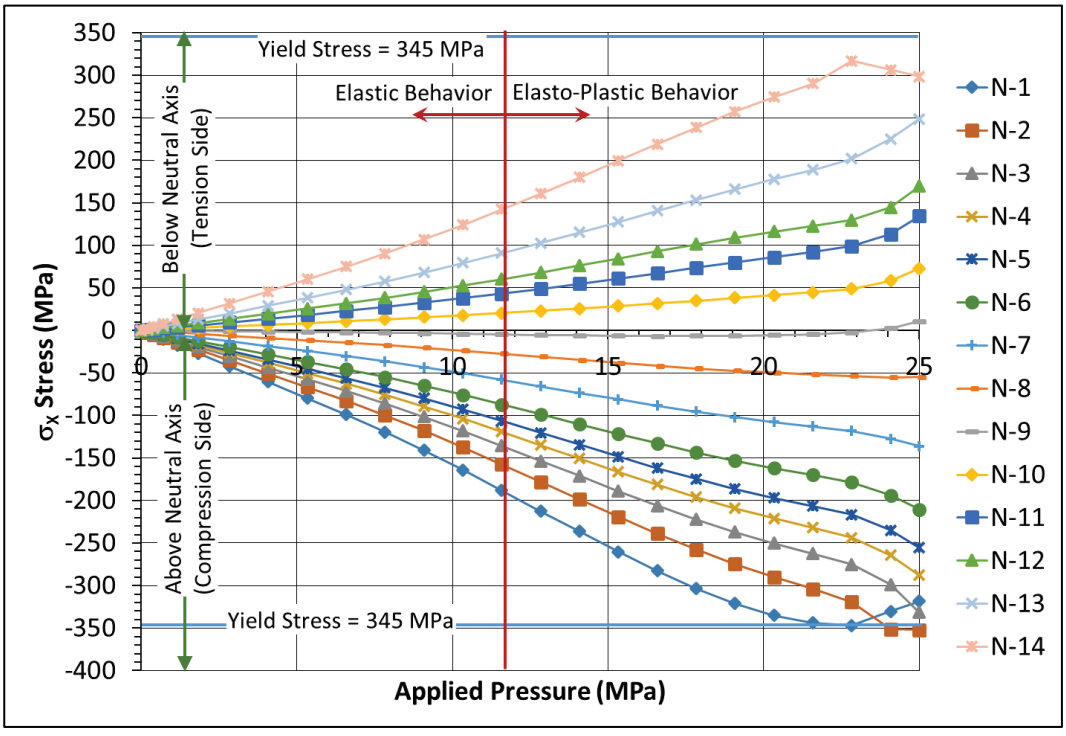

(b)

In Figure 29 a and b, it is also noticed that N-8 is at the neutral axis for σ_Z stresses while N-9 is at the neutral surface for σ_X. However, their corresponding von Mises stresses (Figure 28) are very close to each other, and they crossed as reaching the maximum applied pressure. This crossing can be attributed to the redistribution of stresses. In Figure 29 b, stresses for N-9 change from negative to positive at the maximum applied pressure. In both figures all the stress curves are linearly varying with the applied pressure until the material and the geometrical nonlinearity start to occur. Then the stresses start to redistribute to the other regions of the section that are in the elastic zone. Evidence of this behavior is observed by the larger rate of increment that occurs to the stress diagrams. This is occurring after an applied pressure of 20 MPa. Excessive deformation of a fixed flat structure not only exhibit flexural stresses but also it has a degree of membrane action. The behavior exhibited by the rostrum depicted in these figures is similar to a two-way slab.

3.4.2 Point A

Figure 30 presents a cut of the rostrum at Point A (see Figure 26). This location is to the left side of the rostrum (left of the previously discussed center section) when it is observed from the tip or the end opposite to the fish mouth, at approximately 23 mm from the rostrum edge along a line perpendicular to the z-axis. This section cut includes only tissue (green color) and primary cartilage (red color). This section is thinner and less stiff than the center of the rostrum. It is in a zone where most of the yielding occurs. The figure shows the location of the vertical path used to extract stresses as a function of the vertical location through the thickness. This path starts at the bottom surface of the rostrum (y-axis) and ends at the top surface. The figure also shows the location of the nodes used to extract stresses as a function of applied pressure. The location of these nodes are close to the path, but they are not necessarily in it. These nodes are strategically picked to record stresses at key points. N-1, N-5 and N-6 are in the tissue. N-2 and N-4 are at the interface of tissue and primary cartilage. Finally, N-3 is inside the primary cartilage. It is the reference for the following stress plots. At this location, the thickness of the rostrum is near 10.6 mm (0.42 in).

Figure 30. Illustration of the vertical path and node location for point A (Figure 26). (green – tissue, red – primary cartilage, blue – secondary cartilage)

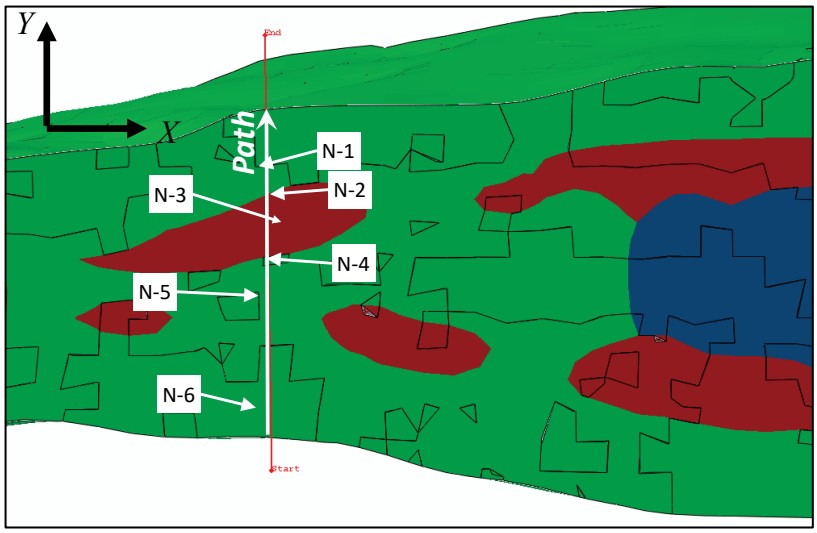

Figure 31 and Figure 32 (a) and (b) show von Mises, σ_x (global x-axis), and σ_z (global z-axis) stresses for selected nodes through the thickness indicated in Figure 30. The stresses are varying as functions of the applied pressure. Yield stress is marked in each figure for reference purposes. Also the applied pressure at which yielding starts (elasto-plastic behavior) is indicated in each figure. Positive stresses in Figure 32 are from the nodes located below the centroid of the rostrum at the tension side and negative stresses are for nodes located above the centroid at the compression side. It is observed in Figure 31 that based on the von Mises stresses and the location of the node along the section, that *N-1* (at the tissue) starts to yield after the applied pressure of 15 MPa (2.17 ksi). It is also observed that nodes N-2 and N-6, which are located almost equidistant from the neutral axis, start to yield after the applied pressure of 17.5 MPa (2.53 ksi). This behavior is also pointed out in Figure 26d. Node N-3 starts to yield at 19 MPa and N-4 after 20 MPa (2.90 ksi). Node N-5, which is near the neutral axis, is close to yielding at the maximum applied pressure of 25 MPa (3.63 ksi). Figure 32 a and b gave a better indication on the stress distributions to each of the axes and their contribution to the section yielding pattern. In both figures, it is observed that N-1 through N-5 are above the neutral axis of the section, with N-*5* very close to the neutral surface. As opposed to the central cut which is very stiff along the z-axis, at this point the behavior is dominated by bending along the x-axis (σ_X), demonstrated by the same yielding patterns of at the nodes that concur with values observed in Figure 31. None of the stresses along the z-axis (σ_X) reached

yielding. From Figure 32 a, it is observed that N-5 has a very low stress value onn the negative side (compression) up to the point in which the section starts to experience significant yielding after 19 MPa (2.76 ksi), and its values start to increase due to the stress redistributions. Similar to von Mises stresses, the σ_X values for N-5 are at yielding at the maximum applied pressure.

Figure 31. Variation of von Mises stresses at selected nodes with applied pressure at point A of the rostrum for the second-order-reduced integration model. (Reference in Figure 30).

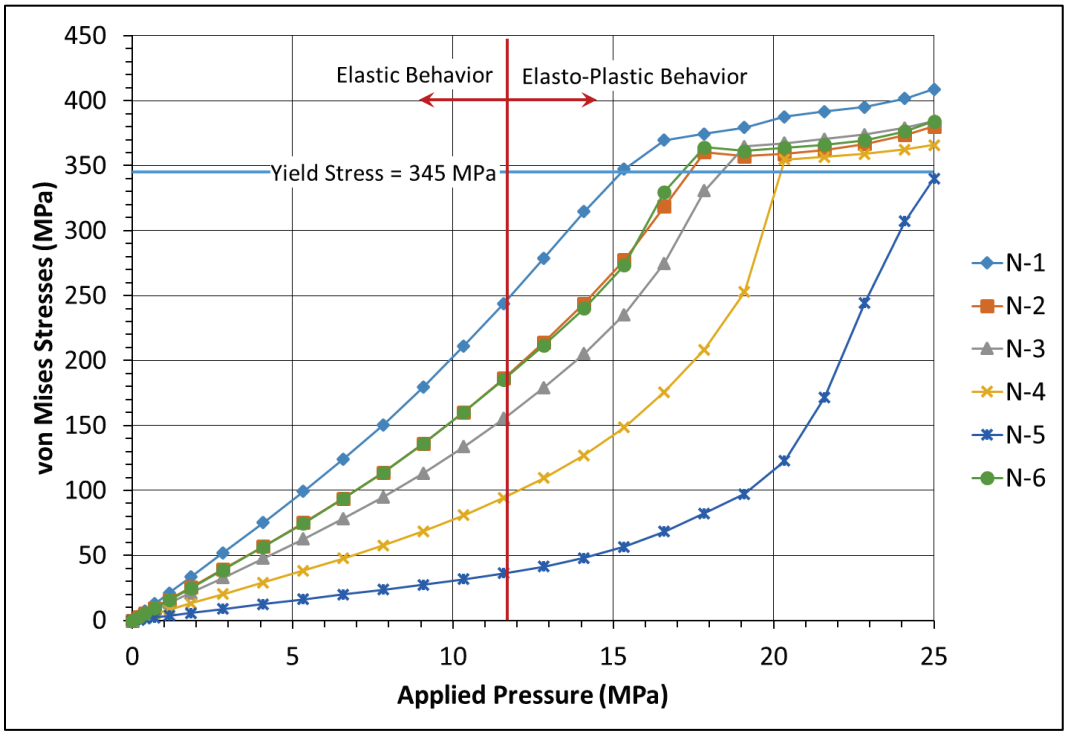

Figure 32. Variation of stresses (a) along the z- and (b) along the x-axes at selected nodes with applied pressure at point A of the rostrum for the second-order-reduced integration model. (Reference in Figure 30).

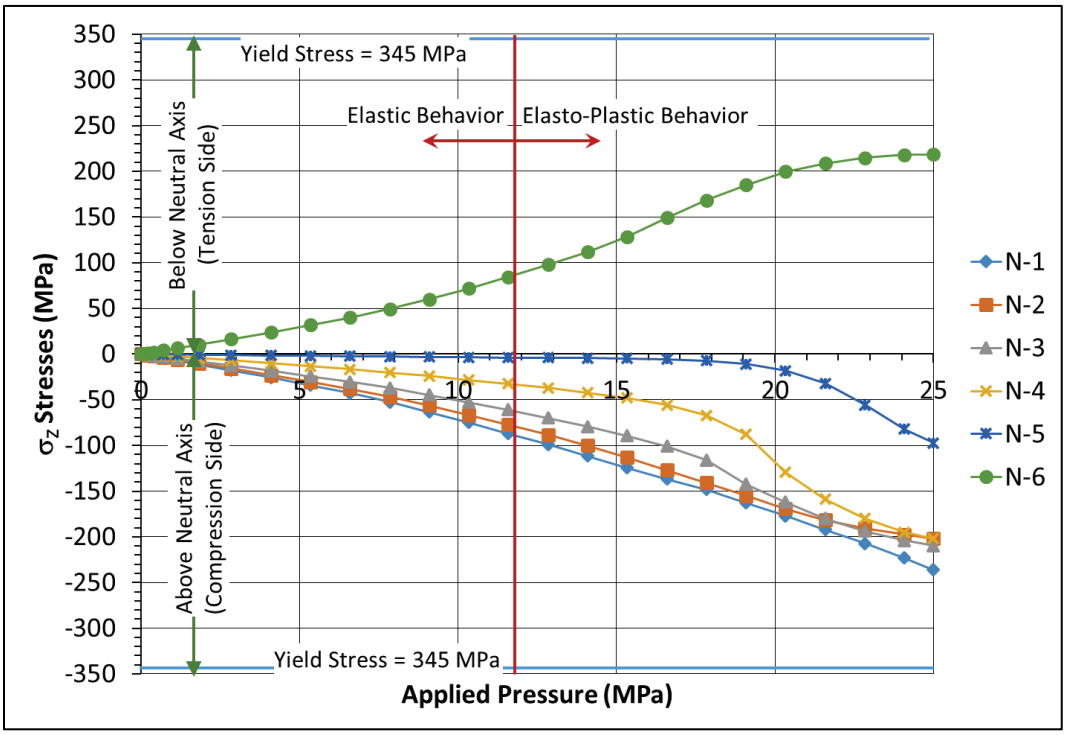

(a)

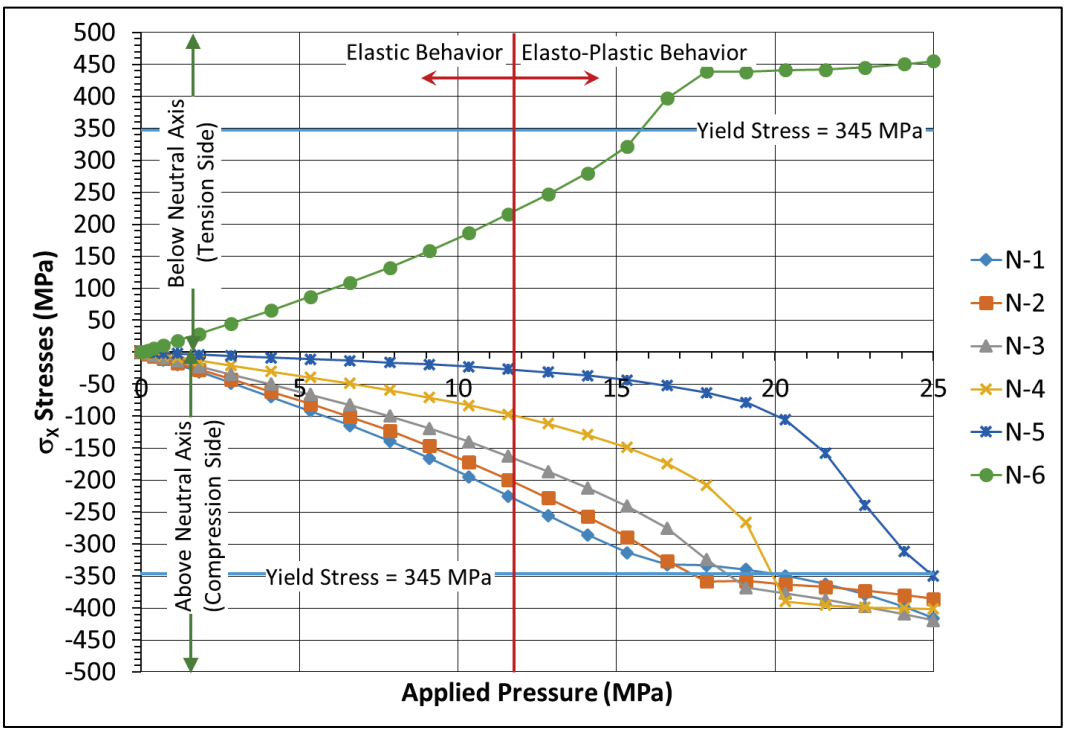

(b)

3.4.3 Cartilages branching from point A

This section discusses results obtained from nodes located at the cartilages that are branching from the cartilage joint referred to as point A (Figure 26). The cross section at the location of the paths using the reference of the local axis (parallel to each cartilage referred as local x-axis) at each point is shown in Figure 35. Each section illustration has a path through the thickness, the number and location of each node used to extract the stresses as a function of the applied pressure and reference to the global coordinate system. Figure 34 shows a top view of the location of the specific primary cartilage for this discussion. The figure also shows the reference local axes with the global coordinate system and the location of each of the cut sections in Figure 33. Similar to the previously discussed locations (center and point A), nodes were selected at the tissue region, inside the cartilages and at the interface between the tissue and cartilage. The list of the nodes and their location using Figure 33 as reference is presented in Table 3. Also the table indicates which nodes of each location is near the neutral surface. Paths along points B, C, and E are crossing only one primary cartilage, thus each section has six nodes except point E that has seven nodes though the thickness. Paths along points D, F, and G are going through two cartilages, thus having nine nodes through the thickness.

The von Mises stresses and σ'_X along each cartilage local x-axis are reported in Figure 35 and Figure 36, respectively. Similar to results from point A, this is a region where most of the yielding is occurring. The figure marks the applied pressure where the section starts to yield. Higher stresses are observed in the direction of the global x-axis as opposed to the center of the rostrum where larger values of stress occur along the global z-axis. The von Mises stresses in Figure 35 indicate that outermost selected nodes reach yielding at applied pressures between 15 and 20 MPa (2.18 and 2.90 ksi). Nodes close to the neutral axis did not reach yielding except in point B (Figure 35a) where N-5 reach yield values after the applied load of 23 MPa (3.34 ksi).

Figure 33. Cross-sectional cuts through each location from point B to G and illustration of the vertical paths and node location for point B (Figure 26). (green – tissue, red – primary cartilage, blue – secondary cartilage)

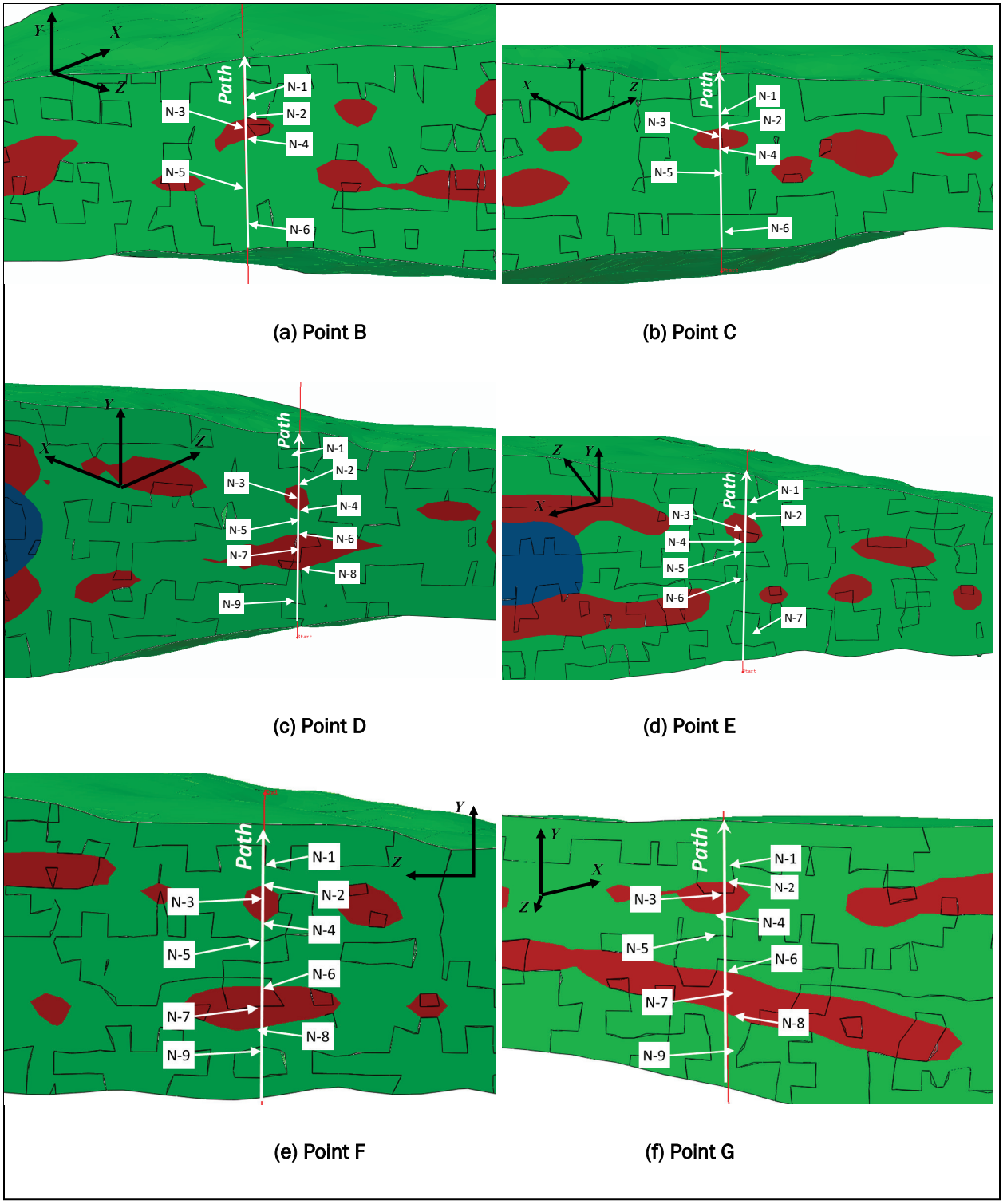

Figure 34. References of local axes of selected primary cartilages (B, C, D, E, F, and G).

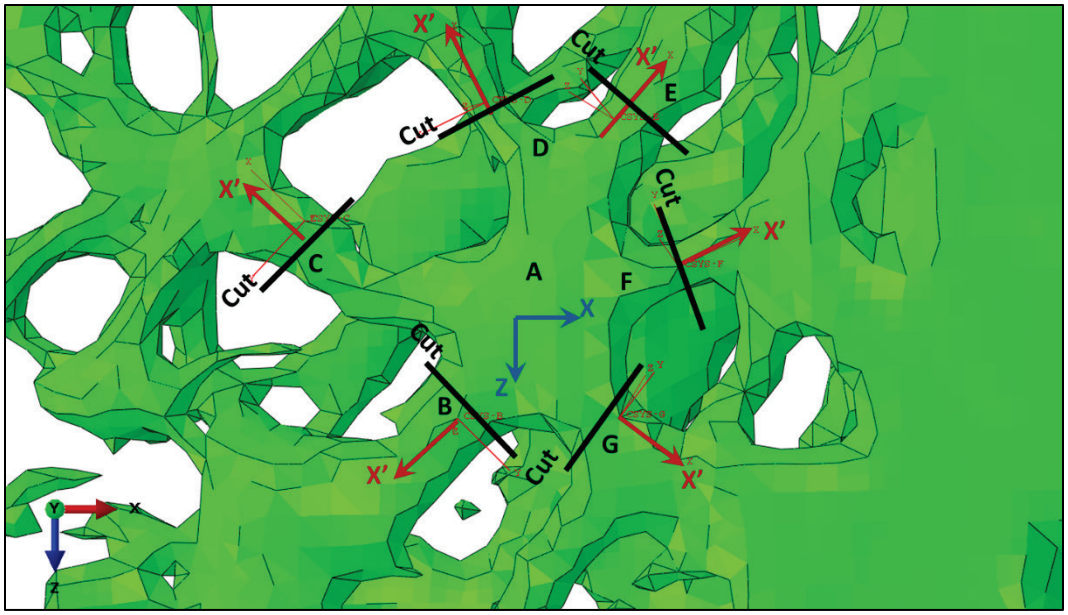

Table 3. Reference nodes locations at cross section.

Location	Nodes per component		
	Tissue	Primary cartilage	Tissue/primary cartilage boundary
Point B	N-1, N-5, N-6	N-3	N-2, N-4
Point C	N-1, N-5, N-6	N-3	N-2, N-4
Point D	N-1, N-5, N-9	N-3, N-7	N-2, N-4, N-6, N-8
Point E	N-1, N-5, N-6, N-7	N-3	N-2, N-4
Point F	N-1, N-5, N-9	N-3, N-7	N-2, N-4, N-6, N-8
Point G	N-1, N-5, N-9	N-3, N-7	N-2, N-4, N-6, N-8
Note: Node number in the grey box are near the neutral surface.			

Figure 35. von Mises stresses of the nodes along the cross sections shown in Figure 33.

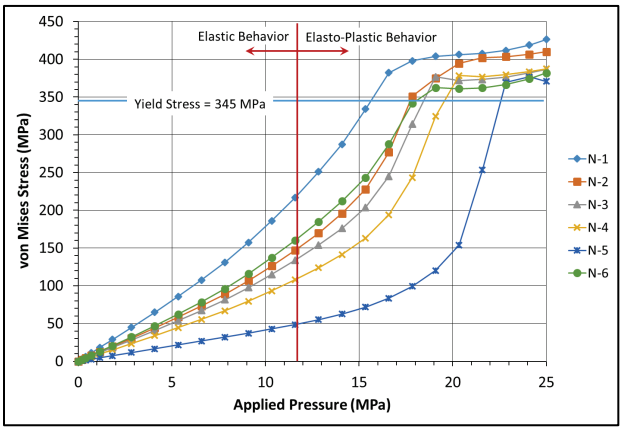

(a) Point B

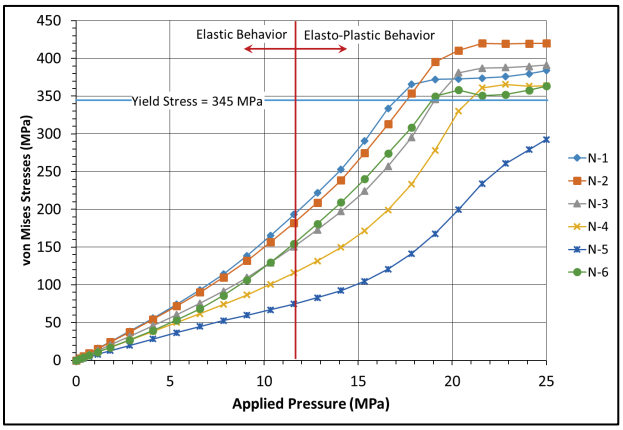

(b) Point C

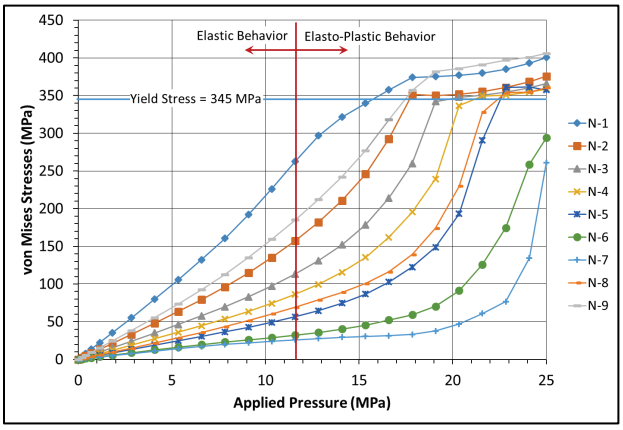

(c) Point D

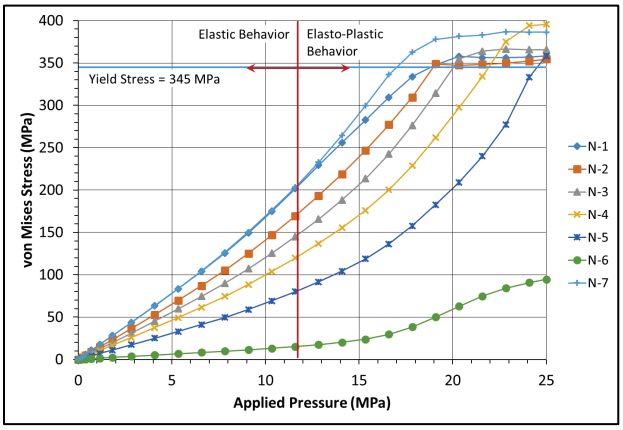

(d) Point E

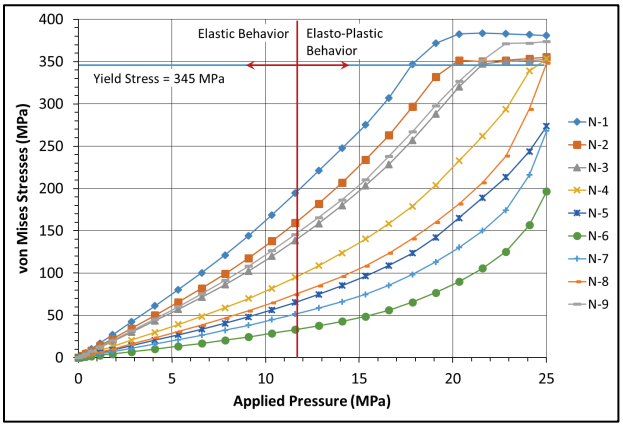

(e) Point F

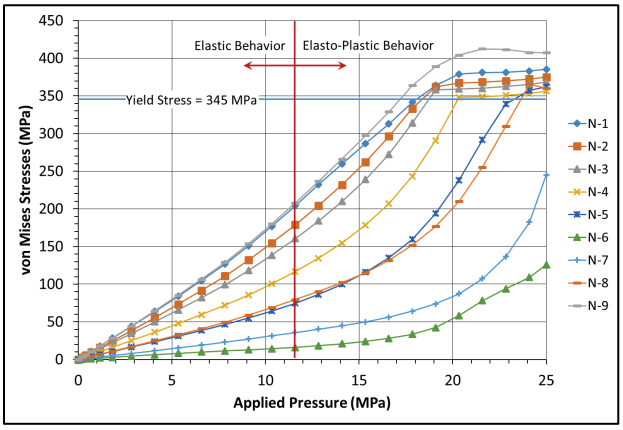

(f) Point G

Figure 36 shows the stresses along a local x-axis in the direction of the cartilage. Since the material is all steel, the stresses along this direction are not necessarily stresses that are transferred through the direction of the cartilage. Depending on the relative orientation of the local x-axis with respect to the global x- and y-axes, it is the level of yielding observed along this direction. If the local x-axis is closer to the global x-axis, the section will show higher levels of yielding (Figure 36a), b, e and f) as opposed to sections with the local x-axis closer to the global z-axis Figure 36c and d), that show no yielding. The local x-axis of Point F is very close to the global x-axis, thus the stress pattern of this section (Figure 36e) is similar to the values in the global axis.

Figure 36. Stresses along the local x-axis (σ'_X) of the nodes along the cross sections shown in Figure 35.

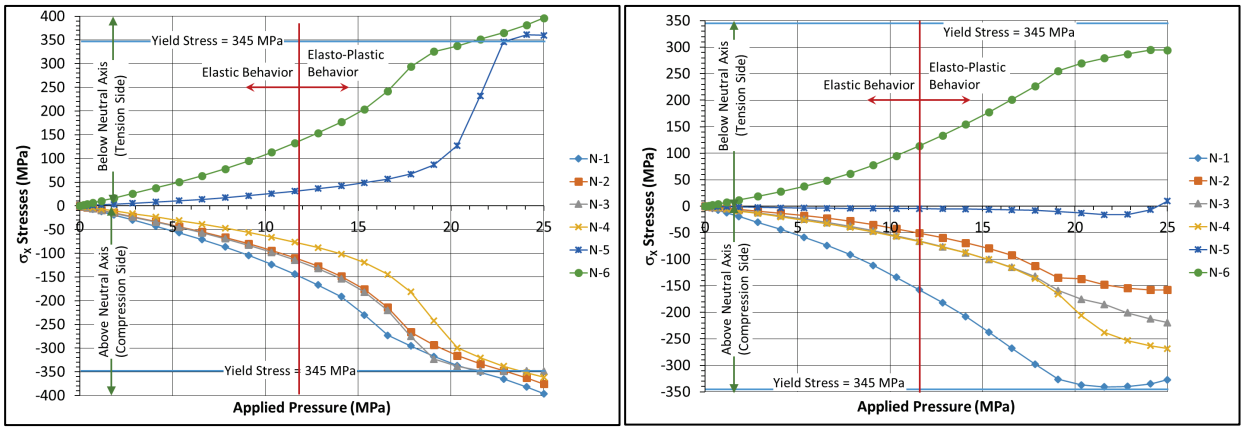

(a) Point B (b) Point C

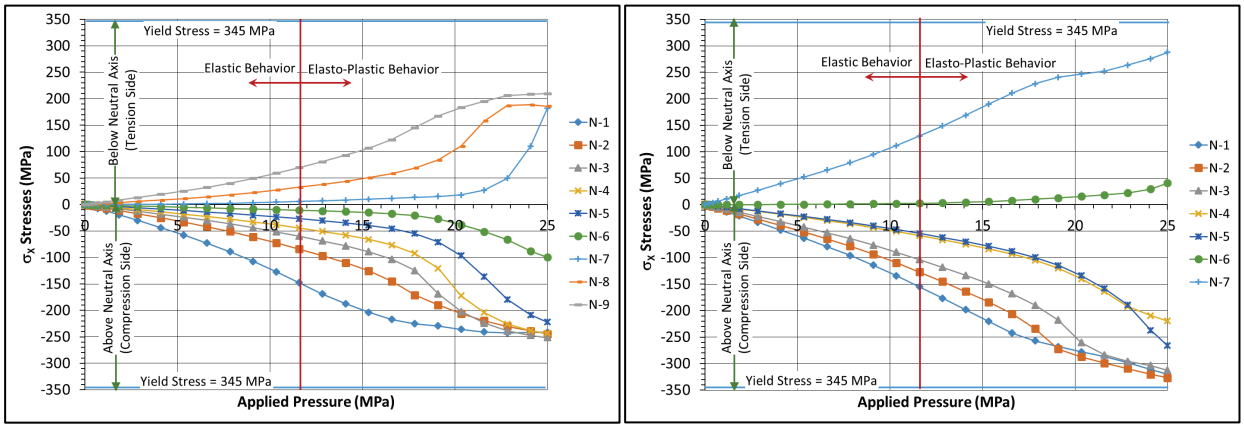

(c) Point D (d) Point E

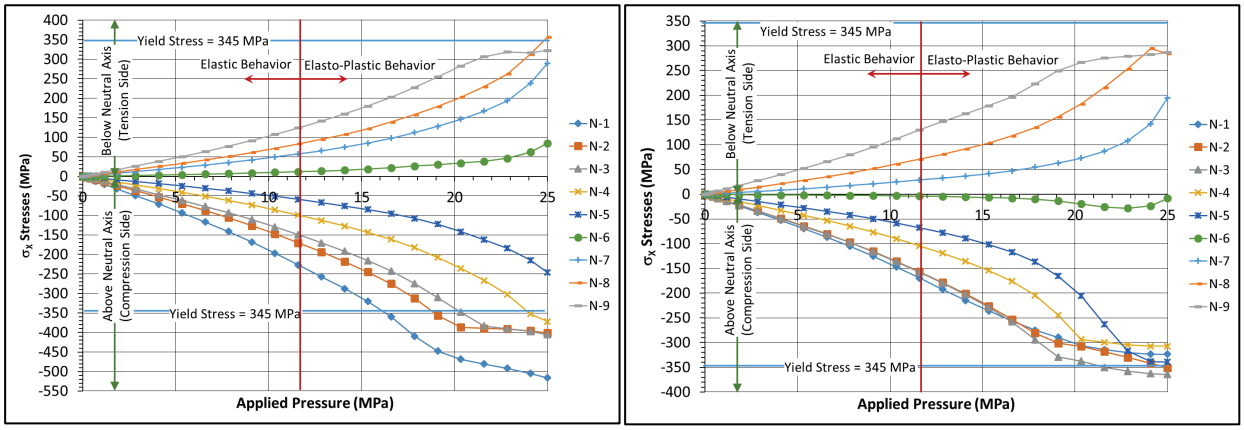

(e) Point F (f) Point G

4 Conclusions

This report presents a comparison of four finite element models of a paddlefish rostrum generated from tomographic scan images. The models considered first-order (linear) elements and second-order (quadratic) elements with reduced and full integration scheme to generate the element stiffness matrices. The material used was steel, considering elastic-plastic behavior. All models were fixed supported at the rostrum edges and loaded by self-weight and gradually to a maximum applied pressure of 25 MPa (3.63 ksi). The models were imported into the commercial software ABAQUS and executed using parallel processing capabilities of the ERDC High Performing Computing facilities.

The literature has general suggestions regarding the general applications of each type of element and integration order. However, selection of the right mesh is problem dependent. From this parametric study it is concluded the following:

- There is not significant differences between integration orders for similar type of elements (first-order or quadratic). This can be attributed to the fact that only hexahedral (brick) elements can have reduced integration orders. Since the models are predominately tetrahedral elements (91.5 percent), they dominate the global model behavior.
- Second-order elements are, in general, more accurate than first-order elements. However, this model does not have experimental data or comparison to validate its accuracy. It is only based on the response of each model with respect to each other. Based on that, then it is concluded that second-order elements with reduced integration are the alternative to analyze biological structures. They can better adapt to the complex natural contours and can model accurately stress concentrations and distributions without over stiffening their general response.
- A drawback to use second-order elements is the increase in computational time and result manipulation, but it can be overcome using modern computing facilities.

The nonuniform geometry of the rostrum creates an interesting behavior when loaded as a fixed plate. The section that connects to the fish is narrower and stiff. The section away from the fish is flat and thinner.

Stresses at the center bone of the rostrum show that even though tissue and cartilages are crossed, the curves are similar to the stress curves of a beam. The stress curves of the zone away from the center cartilage show behavior as plates at the materials' linear range. However at some regions, the curves show non-proportional behavior due to the geometrical nonlinearity of the section. Finally, mesh imperfections created during mesh generation caused irregular stress curves when the elements are change from first-order to second-order.

References

ABAQUS 2014. *ABAQUS Documentation*. Dassault Systèmes: Providence, RI.

Alexander, M.I. 1914. The Paddle-fish (polyodon spathula). *Trans. Amer. Fish. Soc.* 44:73-78.

Allen J.B. and G. A. Riveros. 2013. Hydrodynamic characterization of the polyodon spathula rostrum using CFD. Hindawi Publishing Corporation. *Journal of Applied Mathematics* 2013:346173.

Allison, P.G., M.Q. Chandler, R.I. Rodriguez, B.A.Williams, R.D.Moser, C.A. Weiss Jr., A.R. Poda, B.I. Lafferty, A.J. Kennedy, J.M. Seiter, W.D. Hodo, and R.F. Cook. 2013a. Mechanical properties and structure of the biological multilayered material system, Atractosteus spatula scales *Acta Biomaterialia*. 9 (2): 5289–5296.

Allison, P. G., D.F. Deang, A.J. Diaz, A.R. Poda, J.J. Hoover, M.F. Horstemeyer, and E.J. Perkins. 2013b. Characterization of paddlefish (Polyodon spathula) rostrum stellate bones. *Bioinspired, Biomimetic and Nanobiomaterials* 3(1): 63-68.

Beach, H. 1902. The Paddlefish, Polyodon Spathula. *Bull. Wis. Nat. Hist. Soc.* 2:85-86.

Benzley, S.E., E. Perry, K. Merkley, and B. Clark. 1995. A comparison of al hexagonal and all tetrahedral finite element meshes for elastic and elasto-plastic analysis. *Proceedings of the 4th International Meshing Roundtable, Sandia National Laboratories*. 179-191.

Bright, J.A. and E.J. Rayfield. 2011. The response of cranial biomechanical finite element models to variations in mesh density. *The Anatomical Record* 294: 610–620.

Cheung, J. T-M., M. Zhang, A. K-L. Leung, Y-B. Fan. 2005. Three-dimensional finite element analysis of the foot during standing-a material sensitivity study. *Journal of Biomechanics* 38: 1045-1054.

Cook, R.D., D.S. Malkers, and M.E. Pleshu. 2002. *Concepts and applications of finite elements 4th ed.* Wiley: New York.

Deang, J.F., P. G. Allison, R. Prabhu, L. N. Williams, H. Rhee, W. R. Whittington, E. J. Perkins, S.M. Bruce, and M.F. Horstemeyer. 2017. Constitutive behaviour of paddlefish (Polyodon spathula) cartilage. *Bioinspired, Biomimetic and Nanobiomaterials* 6 (4): 236-243.

de Oliveira, B.L. and J. Sundnes. 2016. Comparison of tetrahedral and hexahedral meshes for finite element simulation of cardiac electro-mechanics. *Proceedings of the VII European Congress on Computational Methods in Applied Sciences and Engineering*. M. Papadrakakis, V. Papadopoulos, G. Stefanou, V. Plevris (ed.), pages: 14.

Dumont, E.R., J. Piccirillo, and I.R. Grosse. 2005. Finite-element analysis of biting behavior and bone stress in the facial skeletons of bats. *The Anatomical Record Part A* 283A: 319-330.

Flammang, B.E. and M.E. Porter. 2011. Bioinspiration: Applying mechanical design to experimental biology. *Integrative and Comparative Biology* 51(1):128-132.

Freutel, M., H. Schmidt, L. Dürselen, A. Ignatius, and F. Galbusera. 2014. Finite element modeling of soft tissues: Material models, tissue interaction and challenges *Clinical Biomechanics* 29: 363-372.

Gurgens, C., D.F. Russell, and L. A. Wilkens. 2000. Electrosensory avoidance of metal obstacles by the Paddlefish. *Journal of Fish Biology* 57: 277-290.

Hoover, J., E. Perkins, and P. Allison. 2013a. Structural and material properties of the paddlefish rostrum. *Proceedings to Technical Directors February 2013*. Vicksburg, MS: U.S. Army Engineer Research and Development Center.

Hoover, J.J., E.N. Rayfield, P.G. Allison, G. Riveros, R.R. Patel, and E. Perkins. 2013b. Role of the rostrum in swimming performance of juvenile paddlefish (polyodon spathula). *Proceedings of the American Fisheries Society 143rd Annual Meeting*.

Lubliner, J. 1990. *Plasticity theory*. Macmillan Publishing Company: New York.

M.R. McCurry, A.R. Evans, and C.R. McHenry. 2015. The sensitivity of biological finite element models to the resolution of surface geometry: a case study of crocodilian crania. *PeerJ* (3):e988.

Meyer, F.P. 1960. Life history of Marispometra Hastata and the biology of its host, Polyodon Spathula. PhD diss., Iowa State University.

Patel, R. R. and G.A. Riveros. 2013. Towards development of innovative bio-inspired materials by analyzing the hydrodynamic properties of polyondon spathula (paddlefish) rostrum. ERDC/ITL TR-13-4. Washington, DC: U.S. Army Corps of Engineers.

Sen, D. (2011). Improvement in mechanical properties through structural hierarchies in bio-inspired materials. PhD diss., Massachusetts Institute of Technology.

Sprague, J. W. 1959. Report of fisheries investigations during the sixth year of impoundment of Fort Randall Reservoir, South Dakota. South Dakota Dep. Game Fish Parks Dingell-Johnson Project F-I-R-8.

Tseng, Z.J., J.L. Mcnitt-Gray, H. Flashner, X. Wang, and R. Enciso. 2011. Model sensitivity and use of the comparative finite element method in mammalian jaw mechanics: Mandible performance in the gray wolf. *PLoS ONE* 6(4).

Vepari, C. and D.L. Kaplan. 2007. Silk as biomaterial. *Prog Polym Sci*.32(8-9): 991–1007.

Wilkens, L.A., M.H. Hofmann, and W. Wojtenek. 2002. The electric sense of the paddlefish: A passive system for the detection and capture of zooplankton prey. *Journal of Physiology-Paris* 96: 363–377.

Wilkens, L. A., and M. H. Hofmann. 2007. The paddlefish rostrum as an electrosensory organ: A novel adaptation for plankton feeding. *BioScience* 57: 399-407.

REPORT DOCUMENTATION PAGE

Form Approved
OMB No. 0704-0188

Public reporting burden for this collection of information is estimated to average 1 hour per response, including the time for reviewing instructions, searching existing data sources, gathering and maintaining the data needed, and completing and reviewing this collection of information. Send comments regarding this burden estimate or any other aspect of this collection of information, including suggestions for reducing this burden to Department of Defense, Washington Headquarters Services, Directorate for Information Operations and Reports (0704-0188), 1215 Jefferson Davis Highway, Suite 1204, Arlington, VA 22202-4302. Respondents should be aware that notwithstanding any other provision of law, no person shall be subject to any penalty for failing to comply with a collection of information if it does not display a currently valid OMB control number. **PLEASE DO NOT RETURN YOUR FORM TO THE ABOVE ADDRESS.**

1. REPORT DATE *(DD-MM-YYYY)*	**2. REPORT TYPE**	**3. DATES COVERED** *(From - To)*
May 2019	Final report	

Numerical simulation of biological structures: Paddlefish rostrum

5a. CONTRACT NUMBER

5b. GRANT NUMBER

5c. PROGRAM ELEMENT NUMBER

Felipe J. Acosta, Guillermo A. Riveros, Reena R. Patel, and Wayne D. Hodo

5d. PROJECT NUMBER
465383

5e. TASK NUMBER
KBF746

5f. WORK UNIT NUMBER
AR058

7. PERFORMING ORGANIZATION NAME(S) AND ADDRESS(ES)

U.S. Army Engineer Research and Development Center
3909 Halls Ferry Road
Vicksburg, MS 39180-6199

8. PERFORMING ORGANIZATION REPORT NUMBER

ERDC TR-19-7

9. SPONSORING / MONITORING AGENCY NAME(S) AND ADDRESS(ES)

Military Engineering 6.1 Program
U.S. Army Engineer Research and Development Center
3909 Halls Ferry Road
Vicksburg, MS 39180-6199

10. SPONSOR/MONITOR'S ACRONYM(S)
USACE ERDC

11. SPONSOR/MONITOR'S REPORT NUMBER(S)

12. DISTRIBUTION / AVAILABILITY STATEMENT

Approved for public release; distribution is unlimited.

13. SUPPLEMENTARY NOTES

14. ABSTRACT

The rostrum of a Paddlefish is used as an antenna to detect electrostatic impulses emitted by plankton and also for hydrodynamic stability while feeding. The rostrum is formed by a network of cartilage, tissue, and interlocking star shaped bones called stellate bones. The objective of this work is to study the load transfer mechanisms of the rostrum bone structure. Steel with elastic-plastic behavior is considered in this study as a basic homogeneous material to evaluate the performance of four models using the following elements: first-order reduced integration, first-order full integration, second-order reduced integration, and second-order full integration. From the study is found that second-order formulation resulted in lower structural stiffness as seen by higher displacements and stresses than using first-order formulated elements. Von Mises stresses as well as global stresses along the rostrum and at a particular location and bones were extracted and compared for the second-order-reduced integration model.

15. SUBJECT TERMS

Paddlefish, Computational mechanics, Rostrum, Bio-inspired materials
Bones, Plankton,
Numerical analysis-Data processing
Hydrodynamics

16. SECURITY CLASSIFICATION OF:			**17. LIMITATION OF ABSTRACT**	**18. NUMBER OF PAGES**	**19a. NAME OF RESPONSIBLE PERSON Dr. Guillermo A. Riveros**
a. REPORT	**b. ABSTRACT**	**c. THIS PAGE**			**19b. TELEPHONE NUMBER** *(include area code)*
UNCLASSIFIED	UNCLASSIFIED	UNCLASSIFIED	SAR	60	6014155317